The THINICE field campaign: Interactions between Arctic cyclones, tropopause polar vortices, clouds and sea ice in summer

Gwendal Rivière, Julien Delanoë, James Doyle, John Methven, Chris Barrell, Matthew Fearon, Suzanne Gray, Aaron Johnson, Olivier Jourdan, Tom Lachlan-Cope, et al.

BAMS Article

The THINICE Field Campaign: Interactions between Arctic Cyclones, Tropopause Polar Vortices, Clouds, and Sea Ice in Summer

Gwendal Rivière,[a] Julien Delanoë,[b] James D. Doyle,[c] John Methven,[d] Chris Barrell,[e] Matthew Fearon,[f] Suzanne Gray,[d] Aaron Johnson,[g] Olivier Jourdan,[h] Tom Lachlan-Cope,[i] Ian Renfrew,[e] Ryan D. Torn,[j] Ambrogio Volonté,[d] Alexandra Weiss,[i] Meryl Wimmer,[a] Clémantyne Aubry,[b] Antoine Baudoux,[h] Eric Bazile,[k] Daniel Beeden,[i] Miriam Bennett,[e] Kevin Biernat,[l] Cecilia M. Bitz,[m] Edward Blanchard-Wrigglesworth,[m] Sophie Bounissou,[b] Matthew Bray,[g] Tomer Burg,[g] Joseph Burzdak,[g] Steven Businger,[n] Peyton Capute,[j] Christophe Caudoux,[b] Steven Cavallo,[g] Laure Cossalter,[b] Capucine Cozzolino,[b] Hannah Croad,[d] Vincent Douet,[o] Andrew Elvidge,[e] Peter Finocchio,[c] Christophe Gourbeyre,[h] Ben Harvey,[p,d] Kevin Huet,[b] Todd Hutchinson,[q] Russ Ladkin,[i] Kai Marshland,[q] Oscar Martinez-Alvarado,[p,d] Guillaume Mioche,[h] Florian Pantillon,[r] Cameron Paquette,[j] David B. Parsons,[g] Ola Persson,[s] Lea Raillard,[a] Jean-Christophe Raut,[t] Yann Seity,[k] Jérémie Trules,[o] Etienne Vignon,[a] and Xuguang Wang[g]

KEYWORDS:
Atmosphere;
Arctic;
Sea ice;
Clouds;
Jets;
Aircraft observations

ABSTRACT: The THINICE field campaign, based in Svalbard in August 2022, provided unique observations of summertime Arctic cyclones, their coupling with cloud cover, and their interactions with tropopause polar vortices and sea ice conditions. THINICE was motivated by the need to advance our understanding of these processes and to improve coupled models used to forecast weather and sea ice, as well as long-term projections of climate change in the Arctic. Two research aircraft were deployed with complementary instrumentation. The Service des Avions Français Instrumentés pour la Recherche en Environnement (Safire) Aerei da Trasporto Regionale 42 (ATR42) aircraft, equipped with the radar–lidar (RALI) remote sensing instrumentation and in situ cloud microphysics probes, flew in the midtroposphere to observe the wind and multiphase cloud structure of Arctic cyclones. The British Antarctic Survey Meteorological Airborne Science Instrumentation (MASIN) aircraft flew at low levels measuring sea ice properties, including surface brightness temperature, albedo and roughness, and the turbulent fluxes that mediate exchange of heat and momentum between the atmosphere and the surface. Long-duration instrumented balloons, operated by WindBorne Systems, sampled meteorological conditions within both cyclones and tropospheric polar vortices across the Arctic. Several novel findings are highlighted. Intense, shallow low-level jets along warm fronts were observed within three Arctic cyclones using the Doppler radar and turbulence probes. A detailed depiction of the interweaving layers of ice crystals and supercooled liquid water in mixed-phase clouds is revealed through the synergistic

DOI: 10.1175/BAMS-D-23-0143.1
Corresponding author: Gwendal Rivière, griviere@lmd.ens.fr
Supplemental information related to this paper is available at the Journals Online website: https://doi.org/10.1175/BAMS-D-23-0143.s1.

Manuscript received 9 June 2023, in final form 12 September 2024, accepted 7 October 2024

combination of the Doppler radar, the lidar, and in situ microphysical probes. Measurements of near-surface turbulent fluxes combined with remote sensing measurements of sea ice properties are being used to characterize atmosphere–sea ice interactions in the marginal ice zone.

SIGNIFICANCE STATEMENT: Arctic cyclones can span several thousand kilometers and last several weeks, bringing strong winds, clouds, and precipitation across the remote Arctic and affecting the sea ice through wind stress, surface energy budget, and snow cover. Therefore, they play a key role in Arctic weather and climate. Motivated by the need to improve the coupled environmental prediction, the representation of cyclones, and their influence on the rapidly changing Arctic climate, the THINICE field campaign intensively observed several Arctic cyclones in August 2022 by operating two aircraft and launching steerable balloons. Key measurements of fine-scale features within Arctic cyclones are highlighted including low-level jets along fronts, mixed-phase clouds containing multiple layers of supercooled water, boundary layer turbulent fluxes, and sea ice properties beneath the cyclones. The ability of state-of-the-art numerical models, with and without coupling to dynamic sea ice models, in representing these cases and coupled processes is the focus of the ongoing work with an aim to improve prediction capabilities.

AFFILIATIONS: [a] LMD/IPSL, École Normale Supérieure, PSL Research University, Sorbonne Université, École Polytechnique, IP Paris, CNRS, Paris, France; [b] LATMOS/IPSL, UVSQ Université Paris-Saclay, Sorbonne Université, CNRS, Guyancourt, France; [c] U.S. Naval Research Laboratory, Monterey, California; [d] Department of Meteorology, University of Reading, Reading, United Kingdom; [e] School of Environmental Sciences, University of East Anglia, Norwich, United Kingdom; [f] SAIC, Monterey, California; [g] School of Meteorology, University of Oklahoma, Norman, Oklahoma; [h] LaMP, Université Clermont Auvergne, CNRS-INSU, Clermont-Ferrand, France; [i] British Antarctic Survey, Cambridge, United Kingdom; [j] Department of Atmospheric and Environmental Sciences, University at Albany, State University of New York, Albany, New York; [k] CNRM, Université de Toulouse, Météo-France, CNRS, Toulouse, France; [l] National Research Council, Monterey, California; [m] Department of Earth and Space Sciences, University of Washington, Seattle, Washington; [n] University of Hawai'i at Mānoa, Honolulu, Hawaii; [o] IPSL, CNRS, Paris, France; [p] National Centre for Atmospheric Science, University of Reading, Reading, United Kingdom; [q] WindBorne Systems Inc., Palo Alto, California; [r] Laboratoire d'Aérologie, Université de Toulouse, CNRS, UT3, IRD, Toulouse, France; [s] CIRES/NOAA/PSL, University of Colorado, Boulder, Colorado; [t] LATMOS/IPSL, Sorbonne Université, UVSQ, CNRS, Paris, France

1. Introduction

The rapidly changing Arctic climate is one of the most alarming signals of global warming as it is having stark impacts on vulnerable ecological systems and indigenous people, livelihoods and activities through sea ice reduction, permafrost thaw, and ice-sheet melting (Post et al. 2013; Overland et al. 2014; Ford et al. 2021). In that context, changes in the characteristics of Arctic weather systems and their links to sea ice need to be better understood to refine climate change projections and to improve weather and sea ice forecasts in the Arctic. Arctic cyclones (ACs) are the dominant synoptic-scale polar weather systems, and they distinguish themselves from smaller-scale polar lows. They also distinguish from midlatitude cyclones by their tracks, which partly or entirely enter the Arctic region (Zhang et al. 2004; Tilinina et al. 2014; Gray et al. 2021). In recent decades, the summertime Arctic sea ice extent has

decreased dramatically (Meier et al. 2022) and also the marginal ice zone (MIZ; the transitional zone between open sea and dense pack ice) has been expanding leading to large areas where sea ice is more sensitive to external factors like ocean waves than in the past. Examples have been cited in the literature where cyclones have been associated with rapid changes in the sea ice distribution in the Arctic (Brümmer et al. 2008; Inoue and Hori 2011; Itkin et al. 2016) and Antarctic (Vichi et al. 2019) associated with wind forcing, cloud cover, and enhanced melting. However, there are many competing processes at play and prediction of these situations is very uncertain.

ACs in summer tend to be of larger scale than in winter, with diameters up to several thousand kilometers and having a lifetime varying between a few days to 2 weeks (Serreze and Barry 1988; Simmonds and Rudeva 2014). Regions of AC activity also differ between the seasons with the local maximum in activity over the central Arctic Ocean in summer disappearing in winter (Serreze and Barrett 2008).

The processes leading to the development and evolution of ACs are not fully understood, and a large part of our knowledge is based on reanalysis data, either through case studies (Simmonds and Rudeva 2012; Aizawa and Tanaka 2016) or statistical analysis using cyclone tracking algorithms (Serreze 1995; Tilinina et al. 2014; Zhang et al. 2004; Vessey et al. 2020). Similar to midlatitude cyclones, the initiation and development of ACs are triggered by baroclinic growth (Gray et al. 2021) and cyclogenesis regions are closely related to large thermal gradients like the Arctic frontal zone (AFZ; Serreze et al. 2001; Day and Hodges 2018) located along the coast of the Arctic Ocean in summer. However, ACs also have noticeable differences from midlatitude cyclones. After their baroclinic growth phase, summertime ACs often become approximately axisymmetric, cold-core structures with cyclonic circulation increasing from the surface to the tropopause and lasting from several days up to 2–3 weeks (Tanaka et al. 2012; Vessey et al. 2022; Croad et al. 2023b). The importance of tropopause polar vortices (TPVs) in the deepening of ACs was highlighted in the case study of a strong cyclone in the summer of 2012 over the central Arctic Ocean (Simmonds and Rudeva 2012). A recent climatology showed that about one-third of ACs are initiated in the vicinity of a preexisting TPV (Gray et al. 2021).

At smaller scales, the life cycles of fronts and low-level jets (LLJs) within ACs and the role they play in strong surface winds, boundary layer stability, and driving turbulence also need to be better understood (Jakobson et al. 2013; López-García et al. 2022). While there have been previous field campaigns examining the evolution of sea ice and role of atmospheric forcing, some of them including ACs (Ruffieux et al. 1995; Brümmer et al. 2008; Persson 2012; Itkin et al. 2016; Persson et al. 2017, 2018; Shupe et al. 2022), to date there have been no field experiments dedicated to the study of ACs and their interaction with sea ice, mediated by the turbulent fluxes between them.

The forecast skill for ACs appears to be generally lower than for midlatitude cyclones (Yamagami et al. 2018a; Capute and Torn 2021), potentially related to insufficient observations to constrain the Arctic circulation (Yamazaki et al. 2015; Yamagami et al. 2018b). The forecast skill for surface cyclones may depend on the ability of models to represent TPVs and processes maintaining them such as radiative cooling associated with the presence of humidity gradients (Cavallo and Hakim 2010). Another explanation for the generally lower forecast skill for ACs could come from the specific interactions between ACs and sea ice and the inaccurate representation of such interactions by numerical models, in particular, over the MIZ. More observations of the Arctic boundary layer are needed to better assess and parameterize turbulent fluxes, in particular, in the presence of LLJs (Vihma et al. 2003; Jakobson et al. 2013). The Year of Polar Prediction site Model Intercomparison Project (YOPPsiteMIP) shows boundary layer temperature biases above ground-based sites (Day et al. 2024); it would be worth investigating such biases above the MIZ in the presence or not of ACs.

ACs are also important to study in the context of climate change because their rapidly changing environment may affect their characteristics (Zhang et al. 2004). Some studies have suggested that their intensity or frequency could increase in summer because of the increased thermal gradients over the AFZ (Day and Hodges 2018) or because of the lower static stability in the presence of sea ice reduction (Mioduszewski et al. 2018; Crawford et al. 2022). Also, ACs play an active role in the Arctic climate by transporting heat and moisture poleward (Persson et al. 2017; Fearon et al. 2021) and participate in the Arctic change, in particular, in the recent records of Greenland snow and ice melting (Oltmanns et al. 2019).

A rather recent debate on ACs has emerged concerning their two-way interaction with sea ice. Several case studies have documented accelerated sea ice disruption and melting over a short period of time associated with ACs (Simmonds and Rudeva 2012; Zhang et al. 2013), but no real consensus has emerged on the general impact of ACs on sea ice (Clancy et al. 2022). This impact depends on the considered months and regions (Aue et al. 2022) and differs between the onset and end of the melting season for instance (Persson 2012; Finocchio et al. 2022). ACs are not systematically followed by rapid sea ice loss events of a few days, but they can induce a weakening of the sea ice structure that may accelerate its disruption and melting later on. Strong winds can create ocean swell and waves that may lead to sea ice edge breakup (Asplin et al. 2012) and enhanced mixing in the oceanic boundary layer leading to an acceleration of the ice melting (Zhang et al. 2013; Smith et al. 2018). Boundary layer processes within ACs are rather complex, and the frictional processes may have different impacts on AC evolution, depending on the warm- or cold-core structure of the ACs (Croad et al. 2023a). In the context of a changing climate where the MIZ extends its surface area, it is even more imperative to improve the representation of momentum and heat exchanges between the atmosphere and the heterogeneous surface of the MIZ in models (Lüpkes et al. 2013; Elvidge et al. 2016; Persson et al. 2018; Renfrew et al. 2019; Elvidge et al. 2021, 2023).

Another major motivation to study ACs concerns the nature of cloud structure, phase, and coupling with cyclone dynamics. Mixed-phase clouds (MPCs) are ubiquitous in the summer Arctic (Mioche et al. 2015) and play an important role in its radiative budget (Shupe and Intrieri 2004). MPCs can appear as a single layer of supercooled water at the cloud top or can consist of multiple stratiform layers of supercooled water (Luo et al. 2008; Morrison et al. 2012; Alexander et al. 2021). MPCs are difficult to represent in numerical weather prediction (NWP) and climate models because the separation between liquid and solid phases usually relies on assumptions that are too strong and are not validated by observations like the temperature-based partitioning (Morrison et al. 2009; Solomon et al. 2011; Sotiropoulou et al. 2016; Kay et al. 2016; Korolev et al. 2017; Hofer et al. 2019; Raillard et al. 2024) and may be a source of uncertainty in the Arctic response to climate change. Arctic clouds have been the research topics of several recent airborne field campaigns such as Arctic Mechanisms for the Interaction of the Surface and the Atmosphere (AMISA; Persson 2010), Arctic Cloud Observations Using Airborne Measurements during polar Day (ACLOUD; Ehrlich et al. 2019) in May–June 2017, airborne measurements of radiative and turbulent fluxes (AFLUX) of energy and momentum in the Arctic boundary layer in the early spring 2019, the Multidisciplinary Drifting Observatory for the Study of Arctic Climate (MOSAiC) Airborne observations in the central Arctic (MOSAiC-ACA) in 2020 (Mech et al. 2022; Shupe et al. 2022), and the High-Altitude Lidar Observatory (HALO)-$(AC)^3$ aircraft campaign in March–April 2022 (Wendisch et al. 2024). Additionally, some surface-based field campaigns like Arctic Summer Cloud Ocean Study (ASCOS; Tjernström et al. 2014) also took measurements of Arctic clouds. However, a large part of these field campaigns were dedicated to boundary layer clouds, and no systematic analysis linking cloud properties and cyclone structure was conducted. In midlatitude cases, the misrepresentation of microphysics in NWP models has been shown

to lead to uncertainties in forecast cyclones (Dearden et al. 2016; Mazoyer et al. 2021, 2023; Oertel et al. 2023). Hence, it is important to study cloud microphysics within ACs.

This paper presents an overview of the THINICE field campaign that was conducted in Svalbard in August 2022 using two aircraft and a balloon platform. The article highlights original observations of the AC structure, embedded fronts, MPCs, sea ice properties, and interactions with TPVs.

2. Scientific questions and objectives of the THINICE experiment

The following scientific questions motivated the design of the THINICE experiment:

- Q1. What processes influence the structure of summertime ACs, including the locations of strongest surface winds and their strength?
- Q2. How do TPVs interact with surface cyclones and what conditions favor the transition from a baroclinic tilted structure to cold-core columnar vortex?
- Q3. Which aspects of AC dynamics and their environment enable some ACs to live much longer than in midlatitudes?
- Q4. How do ACs influence the sea ice surface, including surface stress and surface heat fluxes? What processes contribute to very rapid ice loss events and how are cyclones involved?
- Q5. How do sea ice surface properties affect the dynamics of ACs in summer? How are interactions between ACs and sea ice represented in models with and without dynamic sea ice?
- Q6. What are the characteristics of clouds within ACs and how do they interact? How are clouds within ACs represented in NWP and climate models and what are their feedbacks on AC circulation?
- Q7. What factors influence the predictability of the Arctic weather in summer and how is predictability altered by the presence of ACs, TPVs above, and coupling with the sea ice surface beneath?

The THINICE field experiment had the following observational objectives which were designed to address the above science questions:

- O1. Perform coordinated observations characterizing the AC wind and thermal structure from the tropopause to the surface to determine the dynamical mechanisms responsible for AC development;
- O2. Measure cloud properties on cross sections through ACs, including ice crystals and supercooled liquid layers, as well as liquid cloud and precipitation using airborne radar, lidar, and in situ probes;
- O3. Measure surface layer turbulent fluxes over sea ice, the marginal ice zone, and the open ocean during Arctic summer, particularly within strong winds associated with ACs wherever the lack of cloud allows low-level flying;
- O4. Characterize the sea ice surface (e.g., ice fractional coverage, surface temperature, albedo, and geometric roughness) with simultaneous remote sensing measurements from the aircraft;
- O5. Use a novel balloon-based observational network to obtain a wide coverage of wind, temperature, and humidity profiles throughout the Arctic, in and around TPVs and ACs.

3. Experimental setup and instrumentation

The THINICE field campaign deployed two aircraft and a novel balloon-based observation network. The two aircraft operated from Longyearbyen (78°14′N, 015°27′E) in Svalbard. One was the Service des Avions Français Instrumentés pour la Recherche en Environnement (Safire)

Aerei da Trasporto Regionale 42 (ATR42) aircraft. It has a maximum range of about 1500 km, a maximum endurance of 4.5 h, and operating up to 7-km height. The other was the British Antarctic Survey (BAS) Twin Otter VP-FAZ aircraft. It has a maximum range of about 1400 km and a maximum duration of 5 h and was mainly flying in the boundary layer and up to 5-km height. The WindBorne (WB) System balloons (https://WindBornesystems.com) were launched from Fairbanks, Alaska, and Longyearbyen, Svalbard. They are long-duration balloons under remote control and flew between 4 and 18 days during THINICE.

Table 1 and Fig. 1 describe the payload of the Safire ATR42 aircraft, which was dedicated to measurements of cloud properties and winds over the whole troposphere. In addition to the core in situ sensors and probes on board the ATR42 (not listed in Table 1 but available here[1]), the aircraft was equipped with both in situ microphysical and remote sensing payloads.

[1] https://www.safire.fr/fr/content_page/safire-utilisateurs/latr42.html.

Table 1. Main instruments on board the Safire ATR42 aircraft during THINICE, in addition to the usual core instruments.

Type	Instrument	Measurements and derived properties
Remote sensing	RASTA: 95-GHz Doppler cloud radar (Delanoë et al. 2013) part of the RALI payload (https://rali.aeris-data.fr)	Doppler velocity (including full Doppler spectrum) and reflectivity from six antennas, three looking up and three looking down. Retrievals of 3D components of the cloud wind and cloud properties like IWC (Delanoë and Hogan 2008; Cazenave et al. 2019).
	BASTA: 95-GHz Doppler cloud radar (Delanoë et al. 2016) part of the RALI payload	Doppler velocity and reflectivity along the horizontal direction on the right-hand side of the aircraft. It allows us to retrieve both cloud and precipitation horizontal fractions and microphysical properties.
	The LNG: airborne lidar system (Bruneau et al. 2015) part of the RALI payload	LNG operates at three wavelengths (355, 532, and 1064 nm), including depolarization at 355 nm. The high spectral resolution and Doppler capabilities are available at 355 nm using a Mach–Zehnder interferometer. Key products are optical parameters of aerosols and clouds as well as along-sight wind.
In situ	Cloud droplet probe (CDP-2) with anti-shattering tips (Lance et al. 2010). Manufactured by Droplet Measurement Technologies Inc.	Forward scattering optical size spectrometer for individual droplets in the size range from 2 to 50 μm. Droplet particle size distribution (PSD) on 30 bins with variable widths (1–2 μm), total number concentration, LWC, extinction coefficient, effective diameter (ED), median mass diameter (MMD).
	2D stereo imaging probe (2DS) with tips designed to minimize shattering (Lawson et al. 2006). Manufactured by Stratton Park Engineering Company Inc.	OAP recording two-dimensional images of the shadow cast by hydrometeors on a 128-diode array with a 10-μm pixel resolution. PSDs of water droplets and ice crystals on 124 size bins from 50 to 1280 μm, total liquid–ice number concentrations, LWC, IWC using mass–diameter relations, maximum diameter, MMD, image catalogs.
	High-speed imaging (HSI) flight probe with antishattering tips. Manufactured by Artium Technologies Inc.	High-resolution cloud particle imager recording a frozen shadow of hydrometeors on a CMOS 2048 × 896 pixels sensor with a 2-μm resolution. Size and images of cloud particles from 10 to 1500 μm.
	High volume precipitation spectrometer (HVPS) with tips designed to minimize shattering (Lawson et al. 1993). Manufactured by Stratton Park Engineering Company Inc.	OAP recording two-dimensional images of hydrometeors on a 128-diode array, with a 150-μm pixel resolution. PSDs of liquid water drops and ice crystals on 125 size bins from 600 μm to 19 mm, ice number concentrations, IWC using mass–diameter relations, maximum diameter, MMD, image catalogs.
	Polar nephelometer (PN1) (Gayet et al. 1997)	Angular scattering intensities of an ensemble of cloud particles with size ranging from a few micrometers to 1 mm. Non-normalized scattering phase function at a wavelength of 800 nm, extinction coefficient, asymmetry parameter.
	Ultra-high sensitivity aerosol spectrometer (UHSAS) (Cai et al. 2008)	Scattering optical size spectrometer for aerosol particles in the size ranging from 0.04 to 1 μm. Aerosol number size distribution is divided into 100 size bins with a 10-nm size resolution, total particle number concentration, and mean diameter.

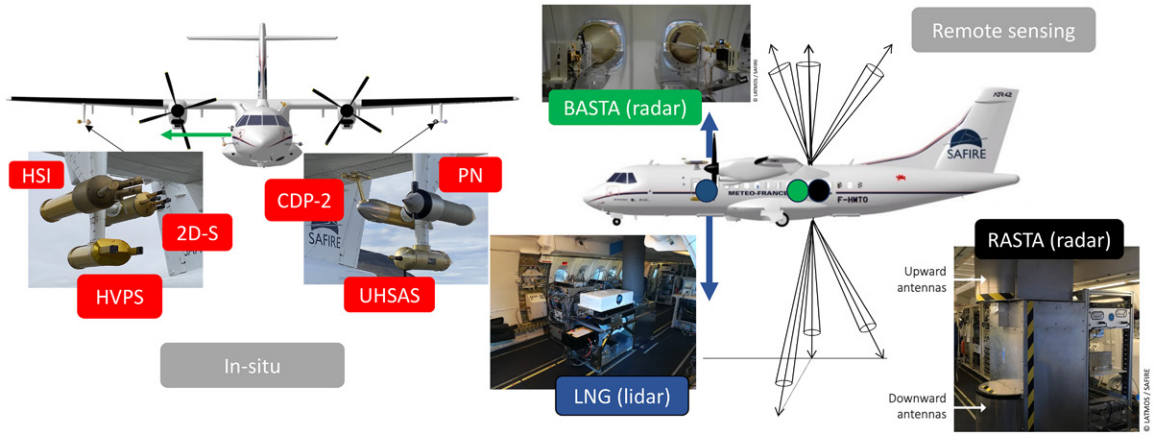

Fig. 1. Schematic of the Safire ATR42 aircraft configuration and payload: (left) in situ microphysical probes are shown in red, and (right) remote sensing instruments (positions of BASTA and RASTA radars and LNG lidar are indicated in green, black, and blue, respectively). Acronyms are defined in Table 1.

The in situ microphysical payload was composed of five microphysical instruments [two optical array probes (OAPs) and one imager, spectrometer, and nephelometer] and one aerosol spectrometer located under the wings as shown in red in Fig. 1. The remote sensing instrumentation was composed of the two Doppler cloud radars Radar System Airborne (RASTA) (black) and Bistatic Radar System for Atmospheric Studies (BASTA) (green) and the high spectral resolution Doppler lidar Leandre New Generation (LNG) (blue). The RASTA radar, thanks to its six antennas pointing in different angles, allows retrieval of the three components of the wind in addition to the reflectivity above and below the aircraft. The sideward looking (right wing) BASTA measures both reflectivity and Doppler velocity with a maximum range of about 12 km and describes the horizontal distribution and properties of both clouds and precipitation. The lidar LNG provides optical parameters of aerosol and clouds and along-sight wind (upward or downward).

The Meteorological Airborne Science Instrumentation (MASIN) equipment on the BAS Twin Otter is summarized in Table 2. Its remote sensing component was composed of a laser altimeter and a radar altimeter to deduce surface height at high resolution, an infra-red thermometer to retrieve surface brightness temperature, and a camera to observe surface and cloud conditions. Its in situ instruments included a turbulence probe, a cloud probe, a dewpoint/frost point hygrometer, a humidity sensor, an aerosol particle counter, and two radiometers to measure upwelling and downwelling short- and longwave radiations (Fig. 2).

WB balloons are small and lightweight and equipped with sensors to measure temperature, humidity, wind, and pressure. In comparison with other long-duration balloon technology, their altitude control in real time enables the measurement of vertical profiles of those meteorological parameters as well as some control of the horizontal track by changing altitude [see more information in Dean and Creus-Costa (2021)].

4. Forecast model setup

During THINICE, several forecast models have been used to plan the flights, the results of two of them are shown in section 6b and compared with observations: one is Météo-France Applications of Research to Operations at Mesoscale (MF-AROME) and the other is Met Office Unified Model, Regional Atmosphere and Land third science configuration (MetUM RAL3). Their setup is hereafter briefly described.

MF-AROME has the same domain as the operational AROME-Arctic used at the Norwegian Meteorological Institute but with a different setup of the parameterization schemes (Køltzow et al. 2019). It was run with a 1.3-km grid spacing, laterally forced and initialized with the operational global model ARPEGE and used AROME-France operational settings (Seity et al.

Table 2. MASIN instruments on board the BAS Twin Otter VP-FAZ aircraft.

Type	Instrument	Measurements and derived properties
Remote sensing	Laser altimeter: Riegl LD90–3800VHS-FLP	Height of up to a few hundred meters, recorded up to 2 kHz.
	Infrared thermometer (IRT): Heimann model KT19.82 and in-flight blackbody calibration target system	Surface (brightness) temperature. Range 8–14 μm, recorded up to 10 Hz.
	Cameras: Gopro Hero7	Video footage and pictures of surface and cloud conditions. A forward looking Gopro is mounted in the cockpit.
	Radar altimeter: Honeywell, KRA 405B	Altitude recorded up to 10 Hz.
In situ	Turbulence probe: NOAA/ARA Best Aircraft Turbulence (BAT) probe combined with thermocouples, probe is fitted on a boom extending forward from the roof of the aircraft	Nine-hole probe records pressures and exposed thermocouple temperatures for measuring turbulence (heat, momentum fluxes) by eddy covariance in conjunction with attitude measurement. Recorded at 50 Hz.
	Cloud, aerosol, and precipitation spectrometer (CAPS) probe	Cloud droplets: 2D imaging probe (25–1550 μm); aerosol spectrometer (0.5–50 μm); LWC probe (0.01–3.0 g m^{-3}).
	Condensation particle counter: TSI 3772 CPC	Aerosol total number concentration.
	Eppley Precision Infrared Radiometer (PIR) (pyrgeometer)	Longwave radiation in both directions as pyrgeometers are fitted to the roof and underside of the aircraft. Recorded at 10 Hz.
	Eppley Precision Spectral Pyranometer (PSP) radiometer (pyranometer)	Shortwave radiation in both directions as pyranometers are fitted to the roof and underside of the aircraft. Recorded at 10 Hz.
	LICOR LI-7000 closed path infra-red gas analyze	H_2O and CO_2. Sampling from Rosemount inlet. Data can be combined with the turbulence probe to determine turbulent latent heat and CO_2 fluxes. Recorded at 50 Hz.
	Pressure sensor, Honeywell HPA	Pressure.
	Humicap, Vaisala	Relative humidity.
	Temperature: Goodrich Rosemount, non-de-iced model 102E4AL, de-iced model 102AU1AG	Total temperature and de-iced and non-de-iced probes mounted on the nose.
	Buck 1011C cooled mirror dewpoint hygrometer	Dewpoint temperature.

2011; Brousseau et al. 2016) coupled to the 1D sea ice model Global Experimental Leads and Ice for Atmosphere and Ocean (GELATO). The MetUM RAL3 was run with a 2.2-km grid spacing nested in the operational Met Office global forecast. Compared to the previous documented configuration RAL2 (Bush et al. 2023), it includes a Bi-Modal cloud scheme and the Cloud Aerosol Interaction Microphysics (CASIM) parameterization (Field et al. 2023).

5. Weather during the field campaign, intensive observing periods, and flights

Unusually intense AC activity occurred during August 2022 in the Svalbard area due to the anomalous poleward position of the North Atlantic jet and its northeastward extension from Iceland to regions of Barents–Kara Seas (Fig. 3). Four ACs were observed during the 4-week field campaign, and their tracks are shown in Fig. 4 using hourly ERA5 output data (Hersbach et al. 2020) and the tracking algorithm of Hodges (1994, 1995, 1999), which uses maxima in spectrally smoothed relative vorticity at 850 hPa. Cyclones 1, 2, and 4 moved northeastward from Iceland toward the Kara Sea, consistent with the zonal wind anomalies. Cyclone 2 is associated with two tracks marking the paths of two distinct vorticity maxima within the same elongated area of low pressure (see Fig. 10). Cyclone 4 is also associated with two distinct tracks, caused by the splitting of the cyclone's low pressure area on 24 August. Durations of cyclones 1, 2, and 4 ranged between 1.5 days (cyclone 1)

Fig. 2. Schematic of the BAS Twin Otter aircraft with the MASIN instrumentation. Acronyms are defined in Table 2.

and 7 days (cyclone 4), typical of midlatitude cyclones. In contrast, the cyclone 3 duration was much longer than the others (13 days). It moved northward over the Greenland Sea, where it interacted with the MIZ, before entering the Arctic Ocean basin and moving over the Arctic pack ice close to the North Pole.

In terms of intensity, cyclone 1 was the weakest with a 999-hPa minimum in mean sea level pressure (MSLP). Cyclones 2, 3, and 4 were of larger scale and deeper with 984-, 990-, and 988-hPa MSLP minima, respectively. While cyclones 1, 2, and 4 kept a well-defined warm sector in the vicinity of their centers, the long-lived cyclone 3, which moved over the MIZ and pack ice, lost its warm sector after 3 days and transitioned to a cold-core vortex extending from the surface throughout the troposphere. This transition from a tilted, baroclinic structure to an untilted, axisymmetric cold-core structure is typical of ACs after peaking in intensity (Croad et al. 2023b). The four observed ACs are hereafter denoted as AC1, AC2, AC3, and AC4.

Flight tracks of the two aircraft and the balloons are shown in Fig. 5. A total of 18 flights corresponding to 80 flight hours were conducted by the BAS Twin Otter aircraft from 29 July to 20 August and 16 flights corresponding to 62 flight hours by the Safire ATR42 aircraft from 5 to 26 August. The WB balloons were launched from two locations and steered by profiling in the vertical wind shear, aiming for profiles into TPV structures throughout the Arctic. WB balloons launched from Svalbard moved eastward without specifically sampling the low-level cyclones observed by the aircraft flights. Many of the WB balloons launched from Fairbanks drifted southeastward and reached the southern Greenland, consistent

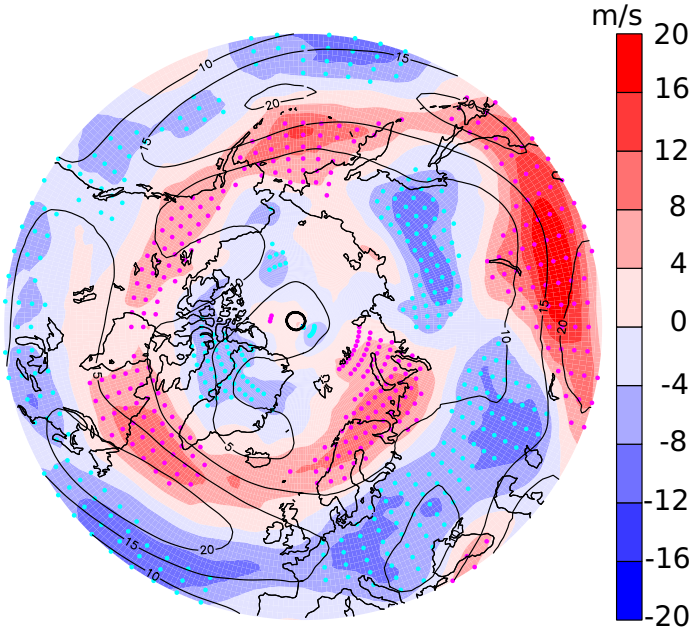

Fig. 3. Zonal wind anomaly at 300 hPa in August 2022 (shadings; m s^{-1}) with respect to the 1979–2022 August climatology (contours; interval: 10 m s^{-1}). Purple and light blue dots, respectively, correspond to positive and negative anomalies larger than the standard deviation. Data from the ERA5 monthly reanalysis with 1° × 1° grid spacing (Hersbach et al. 2020).

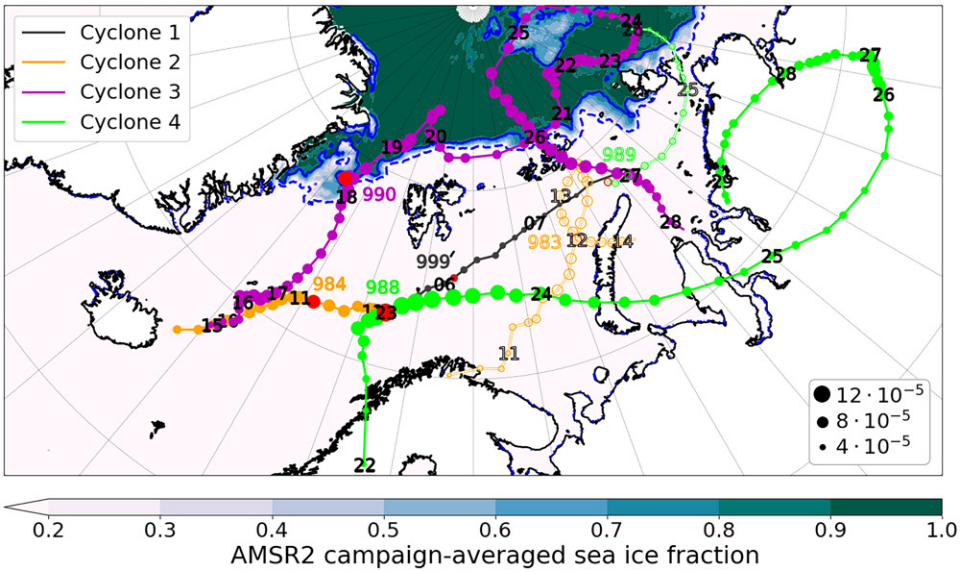

Fig. 4. Tracks of the four ACs observed during THINICE. Cyclone locations are displayed with a 3-hourly frequency. Black date stamps (days in August 2022) are overlaid on the 0000 UTC cyclone location. The location dot size is proportional to the 850-hPa relative vorticity (s^{-1}). Red dots indicate the time of maximum relative vorticity, and the value of minimum MSLP (hPa) at the same time is displayed near the track. Secondary cyclones associated with cyclones 2 and 4 are shown with the same colors as their primary counterparts but with open circles. Tracks and cyclone intensities are based on ERA5 datasets. Advanced Microwave Scanning Radiometer 2 (AMSR2) sea ice fraction (Spreen et al. 2008) averaged between 29 Jul and 25 Aug is shaded, with solid and dashed blue contours, respectively, indicating values of 0.8 and 0.15, the limits of pack and marginal ice.

with the mean wind anomalies of Fig. 3. Some of them reached the Norwegian Sea where ACs 1–4 initiated (Fig. 5c).

AC3 was the most intensively observed cyclone with 10 dedicated flights (see Table 3). Its growth phase was observed on 16 August when a well-defined "bent-back warm front" (i.e., a warm front extending rearwards on the northern flank of the low pressure center and encircling it) was advancing toward Svalbard accompanied by an LLJ peaking at about 30 m s^{-1}. Its mature stage was documented by several flights on 17–19 August. Finally, cold advection associated with AC3 circulation was observed much later on 25 August when the cyclone track returned near Svalbard. The main observed features of ACs 1, 2, and 4 include their warm fronts and associated mixed-phase clouds and LLJs. Besides the four cyclones and their related mesoscale features, other weather phenomena observed during THINICE include orographic tip jets, isolated fronts not associated with a cyclone, and a TPV on 8 August with a weak signature at the surface (see Table 3).

6. Highlights and examples of measurements

Three main facets of the THINICE observations are hereafter highlighted: (i) multilayered mixed-phase clouds along the warm front in AC1, (ii) a strong LLJ running along the cold side of the bent-back warm front in AC2, and (iii) the wind structure of AC3 during its evolution over the MIZ, including its LLJ and TPV above.

a. Mixed-phase clouds along the warm front of AC1. Figure 6 depicts the meteorological situation on 6 August when AC1 reached its maximum intensity. At upper levels (Fig. 6b), the jet stream and the high potential vorticity (PV) band to its north side extended northeastwards from Norway and rolled up into multiple tropopause vortices, one of them being above the surface cyclone. At low levels (Fig. 6a), the weak cyclone is visible southeast of Svalbard (B). By this stage, the cold front (blue curve) and warm sector had run eastward

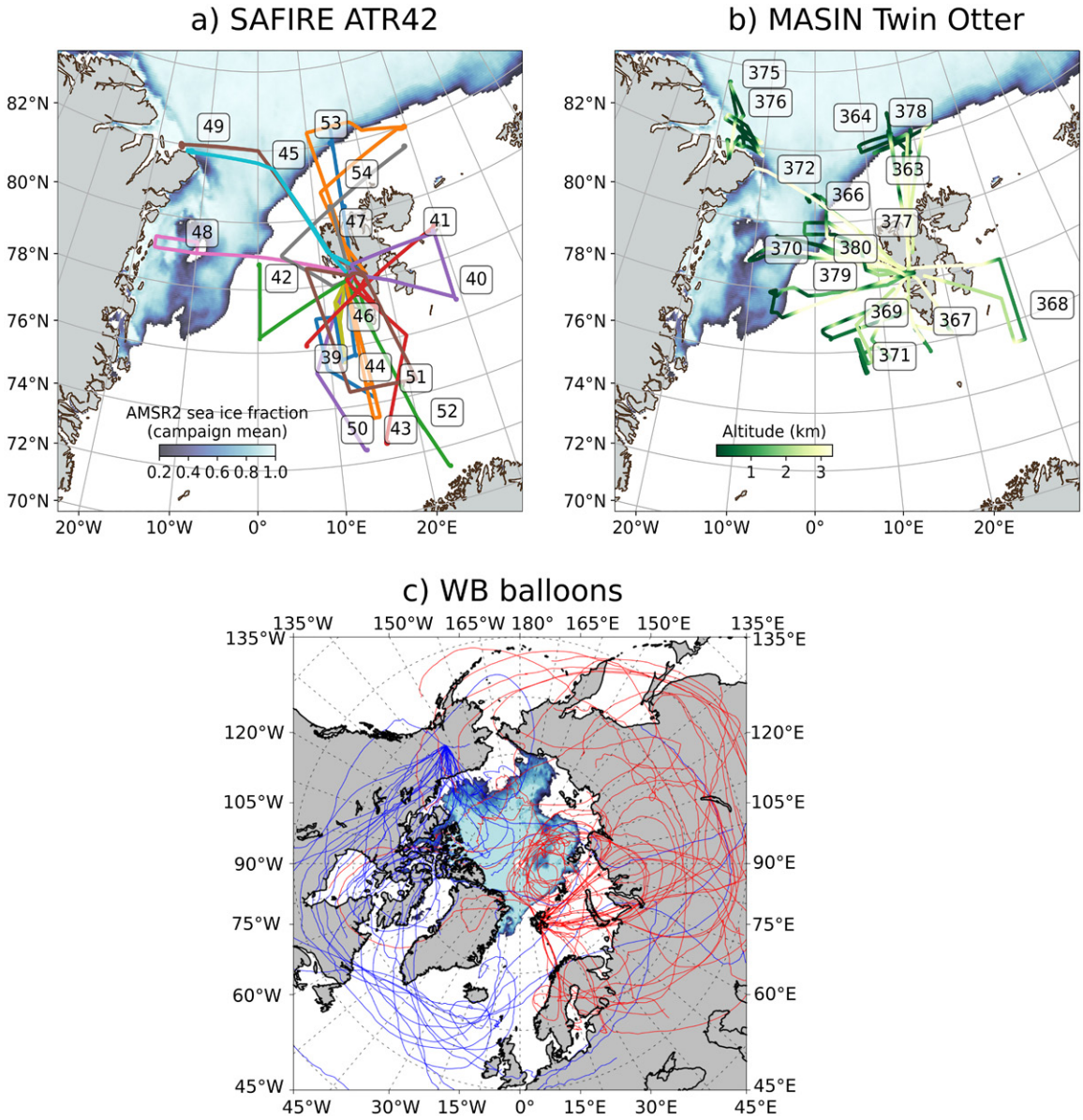

Fig. 5. Flight tracks for (a) Safire ATR42, (b) BAS Twin Otter, and (c) WB balloons (tracks from Fairbanks in blue and from Longyearbyen in red). The AMSR2 sea ice fraction is shown in shadings.

ahead of the cyclone, leaving a weak warm front (red curve) trailing around the northern edge of a uniform warmer temperature across the low center (B). The fronts are marked objectively by following distinct shear lines (vorticity maxima, not shown). Most of the precipitation occurred along the south side of the warm front.

Flights B368 and S40 had a common leg (A–B) flying southward along 29°E to observe clouds across the warm front, starting simultaneously at 78°N, the ATR42 above MASIN. The Safire ATR42 aircraft flew the same leg (A–B–A–B) three times to get vertical profiles of the cloud properties, as shown in Fig. 7. This figure illustrates our strategy for optimizing the observation of mixed-phase clouds: the remote sensing measurements allowed us to identify the area of interest and then fly into the target layer to collect relevant in situ data.

A band of deep clouds (tops ≥ 8 km) above the warm front was crossed three times at 1120, 1210, and 1240 with reflectivity values of up to 15 dBZ (Fig. 7a). South and north of the deep clouds, midlevel clouds were observed with tops varying in altitude from 4 to 5 km and reflectivity values near −10 dBZ. During the whole sequence, the lidar was pointing downward. During the first crossing, when the aircraft flew at a 5.7-km height, the lidar signal was

Table 3. Summary of intensive observing periods, flights, and objectives. Flights serving as illustrations are highlighted.

Weather systems	Dates	BAS flights	Safire flights	Time (UTC)	Objectives
Large-scale ridge and flow onto ice	29 Jul	B363		1125–1655	Sea ice and turbulent flux measurements north of Svalbard
	30 Jul	B364		1054–1614	Sea ice and turbulent fluxes over MIZ to north
	2 Aug	B366		0715–1055	Sea ice and turbulent fluxes over MIZ to NW
Cyclone 1	5 Aug		S39	1329–1658	Clouds on the northern side of cyclone AC1 (weak low)
	6 Aug	B368		1004–1524	Low-level cyclone AC1 structure and cloud at warm front
			S40	1018–1409	MPC on flight stack across precipitating warm front
TPV	8 Aug	B369		0925–1505	Low-level thermal and wind structure beneath a TPV
			S41	1000–1349	Upper-level winds and clouds at the TPV level
Isolated front	9 Aug	B370		0700–1145	Turbulent fluxes over MIZ to the west of Svalbard
			S42	1257–1629	Clouds and LLJ in advancing warm front (upper level)
Cyclone 2	10 Aug		S43	1325–1703	LLJ and MPC along advancing warm front north of AC2
	11 Aug		S44	0655–1057	LLJ along bent-back warm front of cyclone AC2. Jet modulated by orography of southern Svalbard
		B371		0710–1250	Stacked flight legs across LLJ beneath the warm frontal surface
	12 Aug	B372		0700–1135	Turbulent fluxes over MIZ with the weak northerly flow
			S45	1154–1546	MPC over MIZ with the weak northerly flow
Tip jets	2 Aug	B367		1248–1718	Weak easterly tip jet from Svalbard's southern peninsula
	15 Aug	B375		1533–1858	Tip jet northward from Station Nord, Greenland, over MIZ
	16 Aug	B376		0939–1249	Tip jet from Nord (cape) and strong winds over sea ice
Cyclone 3	16 Aug		S46	1230–1648	LLJ and MPC along a strong warm front north of AC3
		B377		1322–1647	Returning to Svalbard into LLJ at the northern edge of AC3
	17 Aug	B378		0800–1240	Winds over MIZ and maturing AC3 structure (transect north)
			S47	1201–1528	Deep clouds in the warm conveyor belt of AC3 (to northeast)
	18 Aug		S48	0901–1253	Northerly LLJ on the western flank of AC3 and cloud head
	19 Aug	B379		0710–1225	Sea ice and turbulent fluxes over MIZ southwest of AC3
			S49	1200–1622	Wind and MPC on the section spanning AC3 and TPV
	20 Aug	B380		1000–1430	Sea ice and turbulent flux measurements over MIZ in a cold air outbreak to the southwest of AC3
	25 Aug		S53	1051–1434	AC3 returns from North Pole. MPC over MIZ and along the cold front on the west side of AC3
			S54	1544–1939	MPC over MIZ and along a cold front west of AC3
Cyclone 4	22 Aug		S50	1054–1445	LLJ along the warm front north of cyclone AC4
			S51	1547–1927	LLJ and MPC along the warm front and convective clouds near cyclone AC4 center
	23 Aug		S52	0734–1139	LLJ along the bent-back warm front and upper-level jets south and north of cyclone AC4

strongly attenuated by cloud particles at the top of the midlevel clouds (Fig. 7b). The strong attenuation at the top of midlevel clouds suggests the presence of supercooled liquid water droplets (see the thin purple layer at 4.2 km between 11:05 and 11:20 in Fig. 7b), while the quasi-non-attenuated signal during the crossing of the deep cloud suggests the absence of liquid (see the green to red area between 1120 and 1130 UTC in Fig. 7b). The latter is confirmed by in situ measurements that do not detect any liquid inside the deep cloud at that altitude and measure ice water content (IWC) ranging from 0.01 to 0.1 g m^{-3} (Fig. 7d). Hydrometeor images show the presence of small dendrites or aggregates and compact ice crystals at that level (leg 1 in Fig. 8).

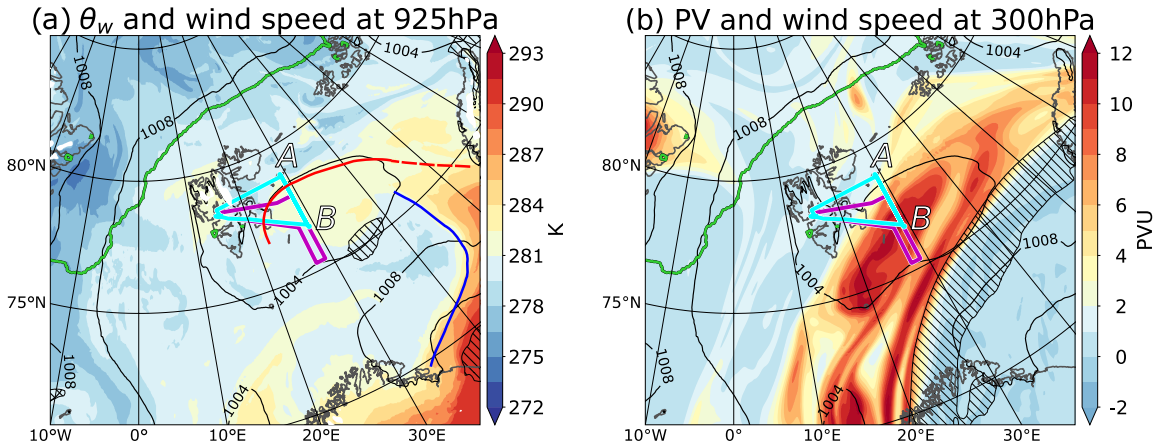

Fig. 6. Cyclone 1 case shown at 1200 UTC 6 Aug 2022 during flights B368 and S40, whose tracks are shown in magenta and cyan, respectively. MSLP (hPa; solid black contours) and sea ice fraction (green contours at 15%) are included in both panels. (a) Wet-bulb potential temperature θ_w (K; shading) and wind speed (hatching above 15 m s^{-1}) at 925 hPa. White masking indicates areas where the model terrain height is higher than the geopotential height at 925 hPa. The main fronts associated with the cyclones are marked (blue lines for cold and red for warm). (b) PV (shading) and wind speed (hatching above 50 m s^{-1}) at 300 hPa. All quantities are from the Met Office global operational analysis data.

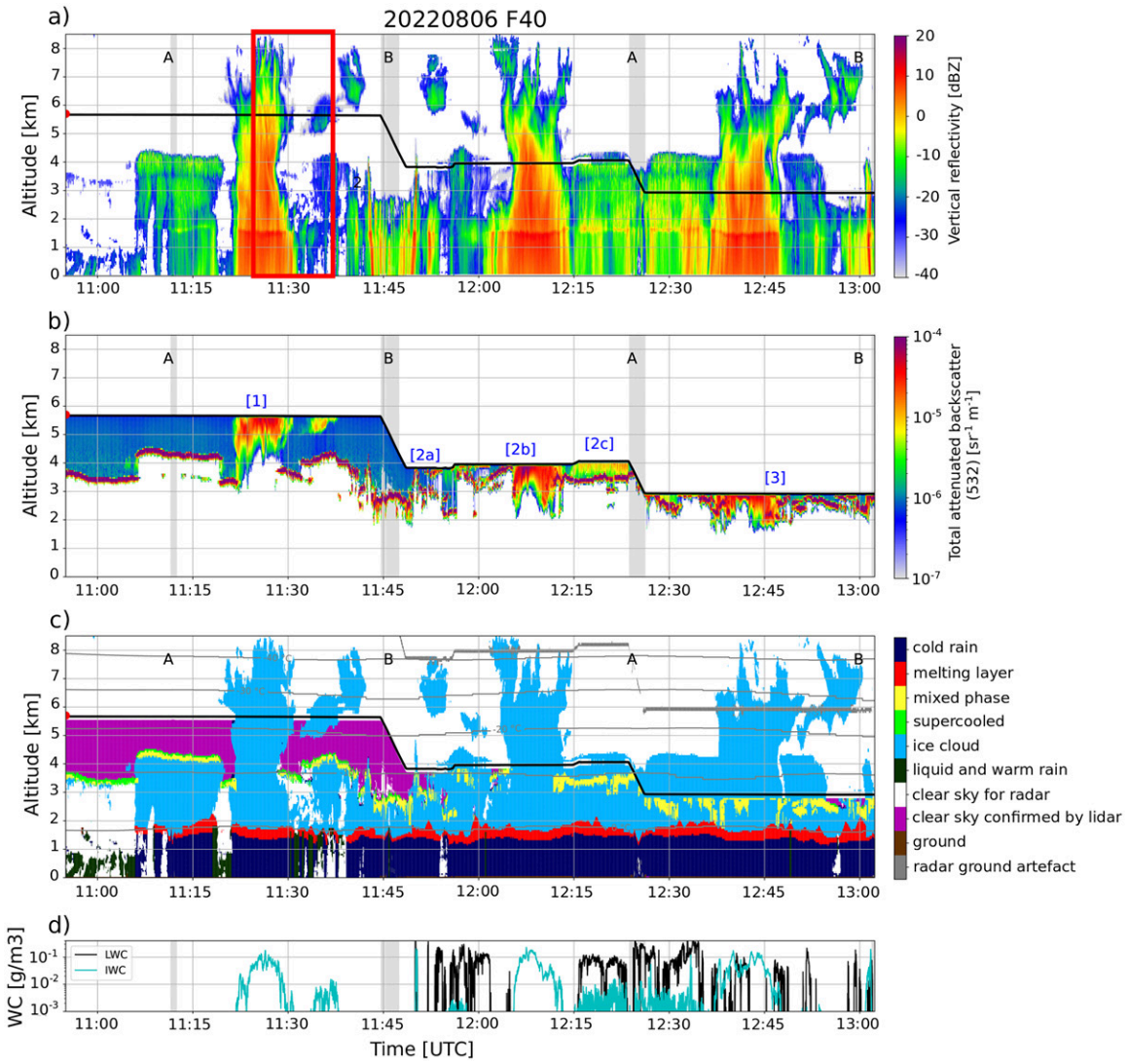

Fig. 7. Cloud properties along legs A–B–A–B of flight S40 on 6 Aug 2022: (a) RASTA vertical reflectivity, (b) LNG attenuated backscatter, (c) cloud categorization, and (d) in situ IWC and LWC as a function of time (UTC) along the S40 flight track. Dashed vertical lines correspond to 180° turning of the aircraft direction.

During the second crossing from south to north, the aircraft level was near the top of midlevel clouds, and the in situ probes confirmed the presence of the supercooled droplet layer that was previously detected by the lidar. Between 1215 and 1225, when the aircraft was at a 4060-m height, images suggest the presence of a few rimed particles and supercooled droplets (leg 2c in Fig. 8). Even though the rimed particles are large, their concentration is low, which would explain the rather small radar reflectivity (–10 dB*Z*). Interestingly, during the same time interval, between 1215 and 1225, the lidar is again strongly attenuated below near 3.5-km height in a thin layer where the radar reflectivity has a local minimum (see the blueish region in Fig. 7a corresponding to the purple band in Fig. 7b). This suggests the presence of another layer of MPCs in which the liquid water content (LWC) reaches values as large as 0.1 g m^{-3}, while IWC is an order of magnitude lower with 0.01 g m^{-3} (Fig. 7d).

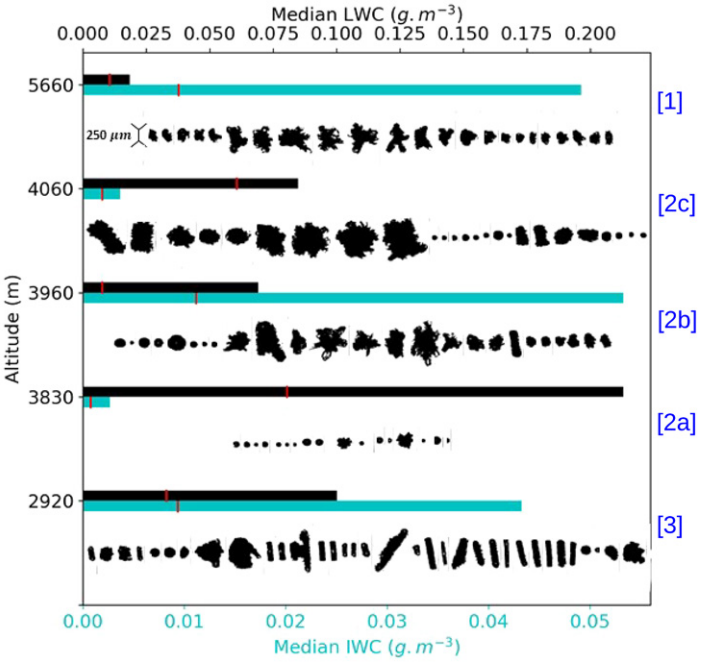

Fig. 8. Hydrometeor images as a function of the mean S40 flight altitudes along legs A–B–A–B. Images are chronologically ordered for each height. Legs 1, 2a, 2b, 2c, and 3 are indicated in Fig. 7b.

During the third crossing, the aircraft was flying southward at a 2.9-km height. Between 1225 and 1235, in situ probes detected a high concentration of liquid and indication of rimed particles is shown on the images (leg 3 in Fig. 8). During that time, the lidar was attenuated by lower layers a few hundred meters below the aircraft. Once the aircraft enters the deep cloud between 1240 and 1245, ice crystals are mainly detected without much liquid with columnar shapes dominating. However, once it leaves the deep cloud near 1247, less ice and more liquid are detected and we again detect the presence of rimed particles.

Figure 9 corresponds to a zoom of the cloud properties when the two aircraft were flying southward along the same leg at 29°E (see the red box in Fig. 7a). The B368 flight level was at a 780-m height, which is below the melting layer, while the S40 flight level was near 5660-m height. The rendezvous of two aircraft at 29°E, 78°N corresponds to the poleward edge of the deep cloud (Fig. 7a). Below the melting layer of the deep cloud (78°–77.7°N), radar reflectivities are high, about 10 dB*Z*, and vertical velocities are near –3 and –4 m s^{-1} (Figs. 9a,b). This indicates heavy precipitation as confirmed by the large drops detected by the CIP B368 probe (Fig. 9c) with mean diameters in the range of 400–600 μm. When the aircraft left the deep cloud near 77.7°N, radar vertical velocities below the melting layer decrease in amplitude as well as the drop mean diameter. Between 77.7° and 77.4°N, the drop mean size decreases near 200 μm, except in some localized regions near 77.5°N, which is consistent with the smaller RASTA vertical velocities of about –1, –2 m s^{-1}, which suggests the presence of a drizzle there. At the end of the common leg (77.4°–77.2°N), precipitation is much weaker as confirmed by both instruments. This comparison between the two distinct measurements on board the two aircraft provides a complementary view of the hydrometeors and precipitation below the melting layer.

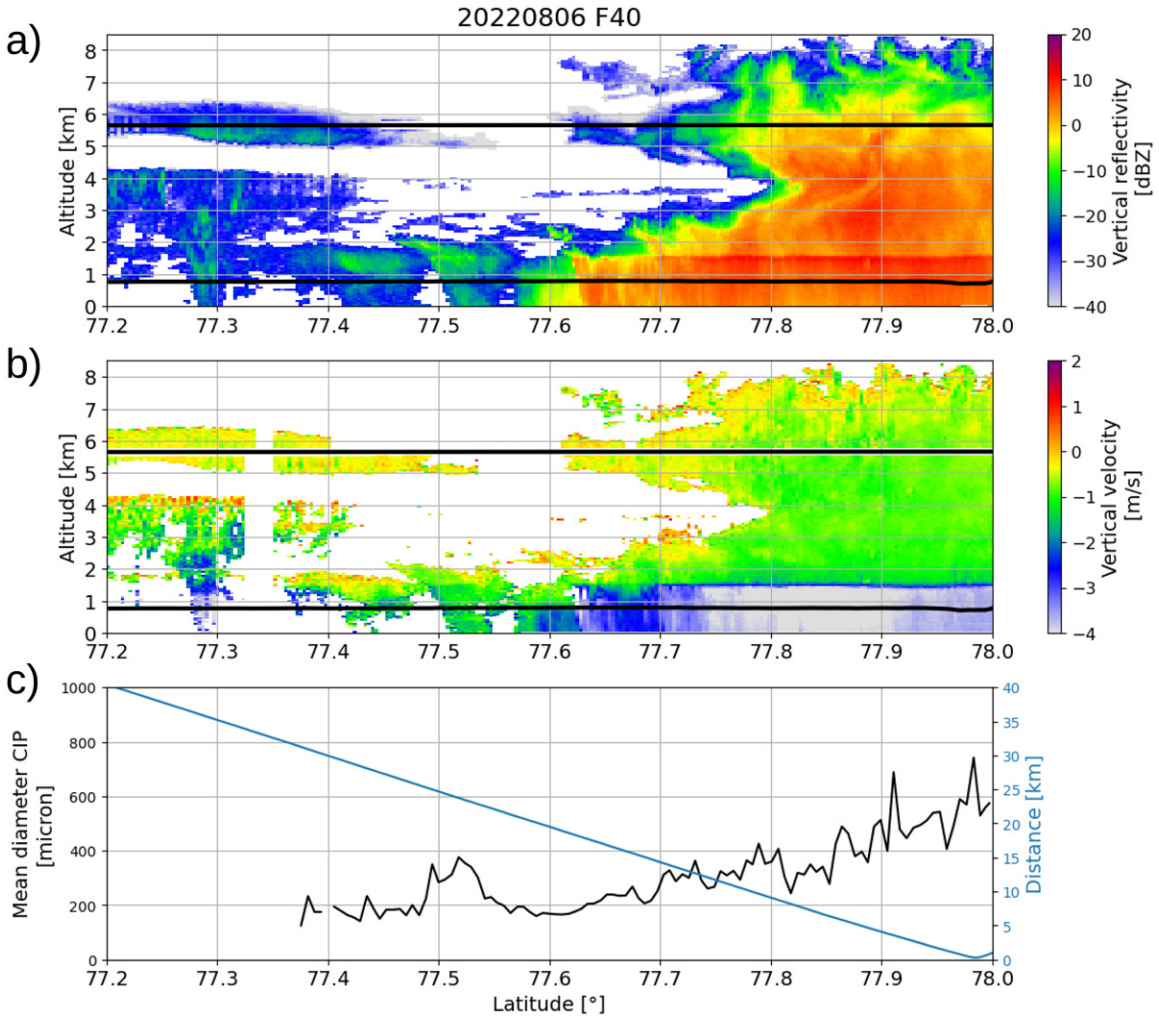

Fig. 9. Zoom of cloud properties along the common leg of flights S40 and B368 on 6 Aug 2022 (see the red box in Fig. 7a): (a) zoom of RASTA reflectivity, (b) zoom of RASTA vertical velocity, and (c) drop mean diameter for drops larger than 100 μm measured by the CIP B368 probe as a function of latitude. Also shown in (c) is the horizontal distance between the two aircraft in blue (ATR42 science speed is faster than MASIN).

To summarize, the complementary radar–lidar and in situ measurements provide a comprehensive picture of the cloud structure north of AC1. The weak warm front itself was characterized by the presence of a narrow, deep, precipitating cloud of about 50–70-km width mostly composed of ice crystals. North and south of the deep cloud, there were midlevel mixed-phase clouds characterized by the presence of multiple layers of high LWC, the first layer being at the cloud top. Thanks to the radar–lidar synergy, cloud categorizations made following the approach developed by Delanoë et al. (2013), Ceccaldi et al. (2013), and Cazenave et al. (2019) are summarized in Fig. 7c. Midlevel clouds include multiple layers of supercooled layers, while deep clouds are mostly ice clouds. However, caution should be taken when interpreting the classification because some regions entering in the "ice clouds" category could include liquid droplets if they are not seen by the lidar.

b. Low-level jet in AC2. AC2 initiated north of Iceland on 9 August (Fig. 4) in the presence of another decaying cyclone south of Iceland. AC2 reached its mature stage and MSLP minimum of 984 hPa at 0000 UTC 11 August, with the two aircraft sampling the system that morning. The zonal jet stream was located over North Scandinavia (hashing in Fig. 10b), with a positive PV anomaly located at its left exit, which is well known to be favorable for cyclone development in midlatitudes (Uccelini 1990). At low levels (Fig. 10a), AC2 displayed

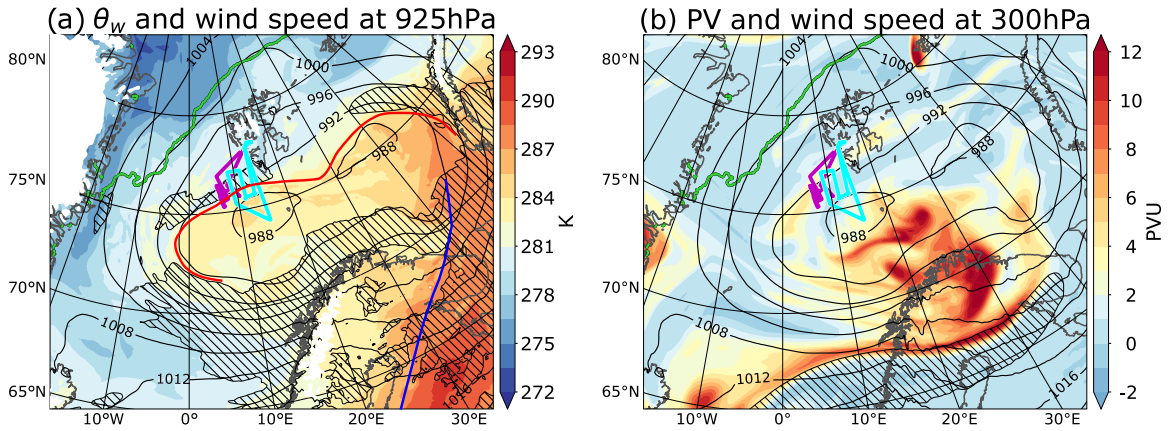

Fig. 10. Cyclone 2 at the time of maximum intensity at 1200 UTC 11 Aug. Same fields as in Fig. 6. Flights B371 and S44 are shown in magenta and cyan lines, respectively.

a zonally stretched MSLP structure with a double surface pressure minimum. The cyclone's warm sector and cold front (blue curve) propagated eastward far ahead of the cyclone. Strong low-level winds occurred around the cyclone on all sides (hashing in Fig. 10a). The westward LLJ in the cold air north of the bent-back warm front (red curve) is characteristic of the "cold conveyor belt" often identified in midlatitude cyclones but is remarkably extended in the zonal direction in this case. Both flights crossed that front several times and measured winds and cloud properties within it, at the time when it reached the southern parts of Svalbard and was likely modulated by some terrain effects.

Flight B371 sampled the LLJ vertical structure southwest of the Svalbard terrain (Fig. 11a), sufficiently far from the terrain to minimize its effects. The westernmost leg of flight S44, denoted as AB in Fig. 11a, was coordinated with the vertically stacked legs between 300 and 3000 m of flight B371 across the bent-back front. The Safire ATR42 flew northward almost directly above the BAS Twin Otter aircraft (near the midpoint of AB) as the latter began a profile downward to 300 m above the sea in the cold air underneath the frontal surface. The front was only moving slowly northward so the B371 measurements can be projected in the alongfront direction onto the same cross-sectional AB. The in situ wind measurements on the BAS Twin Otter aircraft (dots in Figs. 11b,d) and the RASTA radar wind measurements on board the Safire ATR42 aircraft (Fig. 11f) show the LLJ core primarily near and north of the AB midpoint beneath the sloping frontal surface.

The winds and wet-bulb potential temperature θ_w from two short-term 9-h forecasts made using MF-AROME and MetUM RAL3 are shown in Figs. 11a,b and 11c,d, respectively. The frontal gradient in θ_w is more pronounced in the MetUM RAL3 simulation than in MF-AROME. In both cases, the easterly jets are confined to the cold air beneath the sloping frontal surface, as expected from thermal wind balance. In both forecasts, the frontal surface is displaced slightly northward relative to the observation location (Figs. 11d,f) and the LLJ structure is different with the wind maximum extending further north in the MetUM forecast. The peak wind speed values in the observations (22.4 m s^{-1} for flight B371 in Fig. 11e and 25.3 m s^{-1} for the radar RASTA in Fig. 11f) are just above the boundary layer, approximately 500 m above the sea. Both models underestimate wind speed throughout the LLJ by 3–5 m s^{-1} (Fig. 11e), and the underestimation is also present in the ERA5 reanalysis (not shown). The maximum wind speeds anywhere in the LLJ are 16.9 m s^{-1} for MF-AROME and 17.7 m s^{-1} for the MetUM, which is only 70% of the observed maximum. To conclude, the zonal extension and the shallow structure of the LLJ and warm front of AC2 are remarkable. Future studies will investigate processes involved in the maintenance of the LLJ intensity and the reasons for its underestimation in the short-term forecasts and reanalysis.

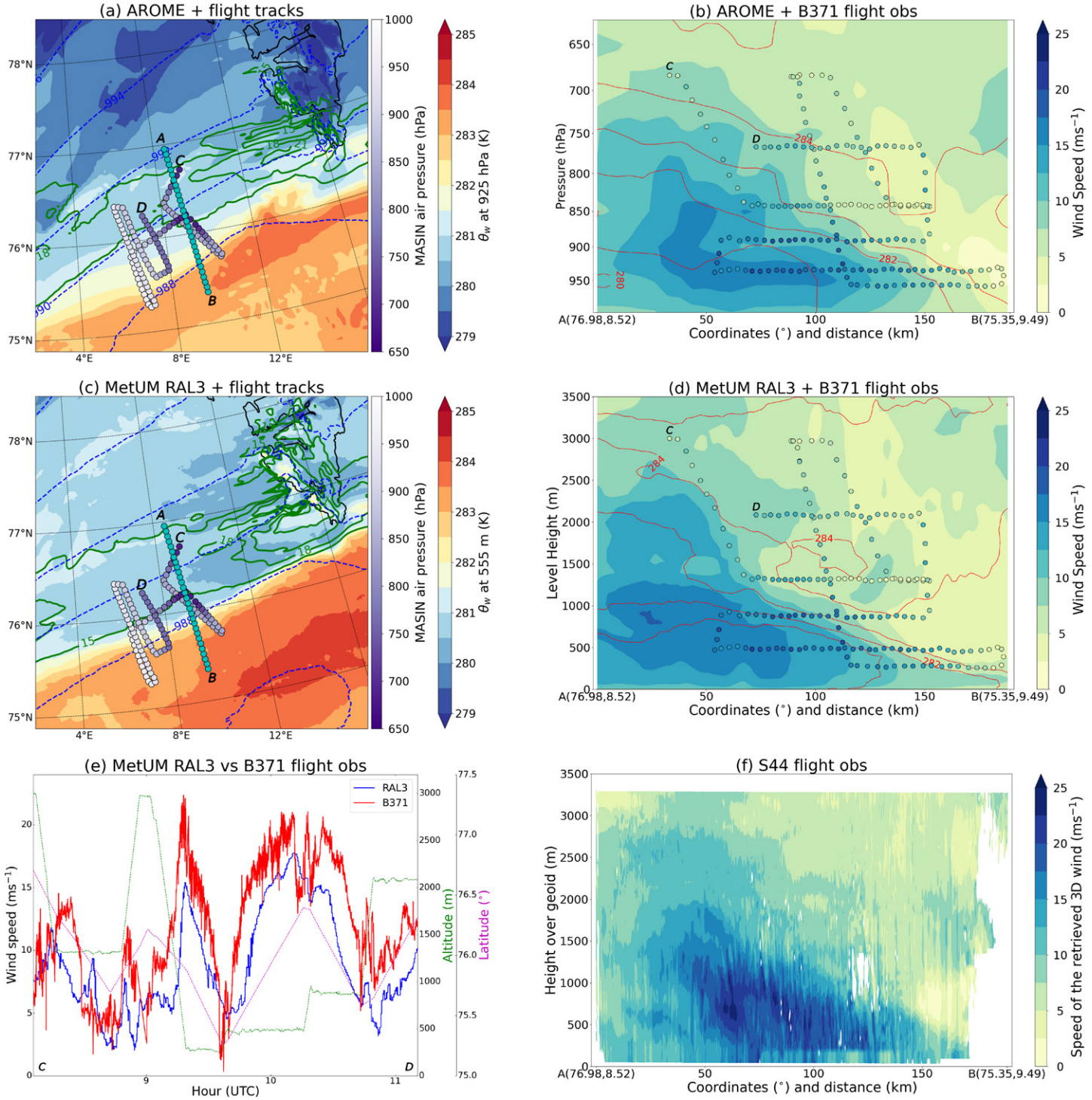

Fig. 11. Observation and model comparison on sections through the bent-back front of cyclone 2. Segments of tracks of flights B371 (purple dots colored by air pressure; hPa) and S44 (cyan dots) overlaid on model data from (a) AROME forecast and (c) MetUM RAL3 forecast valid at 0900 UTC 11 Aug (simulations initialized at 0000 UTC 11 Aug). The maps show θ_w (K; shading) and wind speed (ms^{-1}; green contours) at the model level closest to 925 hPa for MetUM RAL3 and at 925 hPa for AROME and MSLP (hPa; blue dashed contours). The black lines outline the Svalbard terrain. Vertical cross sections of (b) AROME and (d) MetUM RAL3 wind speed (m s^{-1}; shading) and θ_w (K; red contours) along transect AB. Dots indicate wind speed measured by the turbulence probe during flight B371 projected perpendicularly onto this section (m s^{-1}; shading) and displayed every 60 s. (e) Time series of observed (B371, displayed at 1 Hz frequency) and forecast (MetUM) wind speeds (m s^{-1}; blue and red lines, respectively). BAS Twin Otter aircraft altitude and latitude are indicated with green and magenta lines. Observations are compared against model data at the nearest vertical level, horizontal grid point, and time (1-h frequency). (f) Wind speed (m s^{-1}) observed by RASTA Doppler radar during flight S44 on segment AB.

c. AC3 evolution over the marginal ice zone. AC3 formed northeast of Iceland on 14 August (Fig. 4) via the baroclinic interaction with an upper-level high PV anomaly and then moved to the north over the Greenland Sea. By 19 August (Fig. 12b), the upper-level PV anomaly was elliptical and clearly cut off from any other PV features and became almost axisymmetric by 20 August (Fig. 12d)—the characteristics of a TPV. At the same time, at lower levels (Figs. 12a,c), the surface cyclone started to develop a cold core but was still asymmetric, with the airmass from the north on the west cyclone flank being markedly cooler (and drier) than its eastern side. The cyclonic circulation extended through the atmosphere from the surface cyclone to the tropopause, forming a vortex column. Vorticity increased with height (the TPV being associated with stronger winds than the surface cyclone) in thermal wind balance with a cold core at all levels. On 27 August, the vortex column approached a high-latitude jet stream above the Russian coast (not shown) and the TPV was advected rapidly eastward and elongated by shear, destroying the columnar vortex by 28 August.

Several flights were conducted during that transition of AC3 to cold core over the Greenland Sea; two of them are highlighted here. Flight S49 flew on 19 August from southeast to northwest at a 6.5-km height crossing the lower part of the TPV. The ATR42 then performed a spiral descent to the boundary layer near B (1412 UTC; Figs. 12a and 13a) in the presence of strong northerly surface winds (≥20 m s^{-1}). It was followed by a low-level transect returning along the same path to Svalbard via point A. The TPV corresponds to a lowering of the dynamic tropopause to a 6-km altitude [see 2-PVU (PVU; 1 PVU = 10^{-6} K kg^{-1} m^2 s^{-1}) contour in Fig. 13a] flanked by upper-level jets representing the flow around it. To the northwest (point B), the northerly upper-level jet had its peak strength over 25 m s^{-1} near an 8-km height (Figs. 13a,b). The upper-level jet core was mainly above the clouds, which explains why

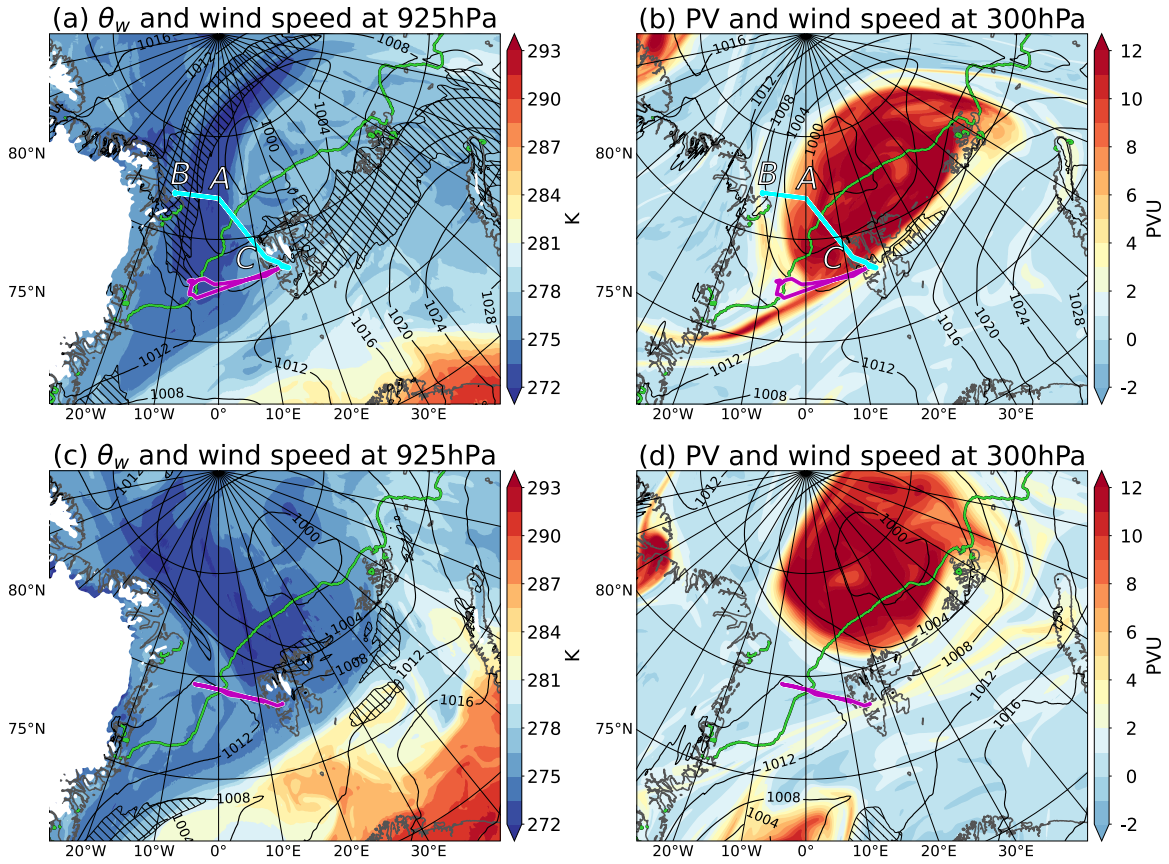

Fig. 12. Cyclone 3 shown at the following times: (a),(b) at 1200 UTC 19 Aug, with flights B379 and S49 shown in magenta and cyan lines, respectively (A and B markers indicate the transect shown in Fig. 13); (c),(d) at 1200 UTC 20 Aug, with flight B380 shown in magenta. Same fields as in Fig. 6, but without front lines.

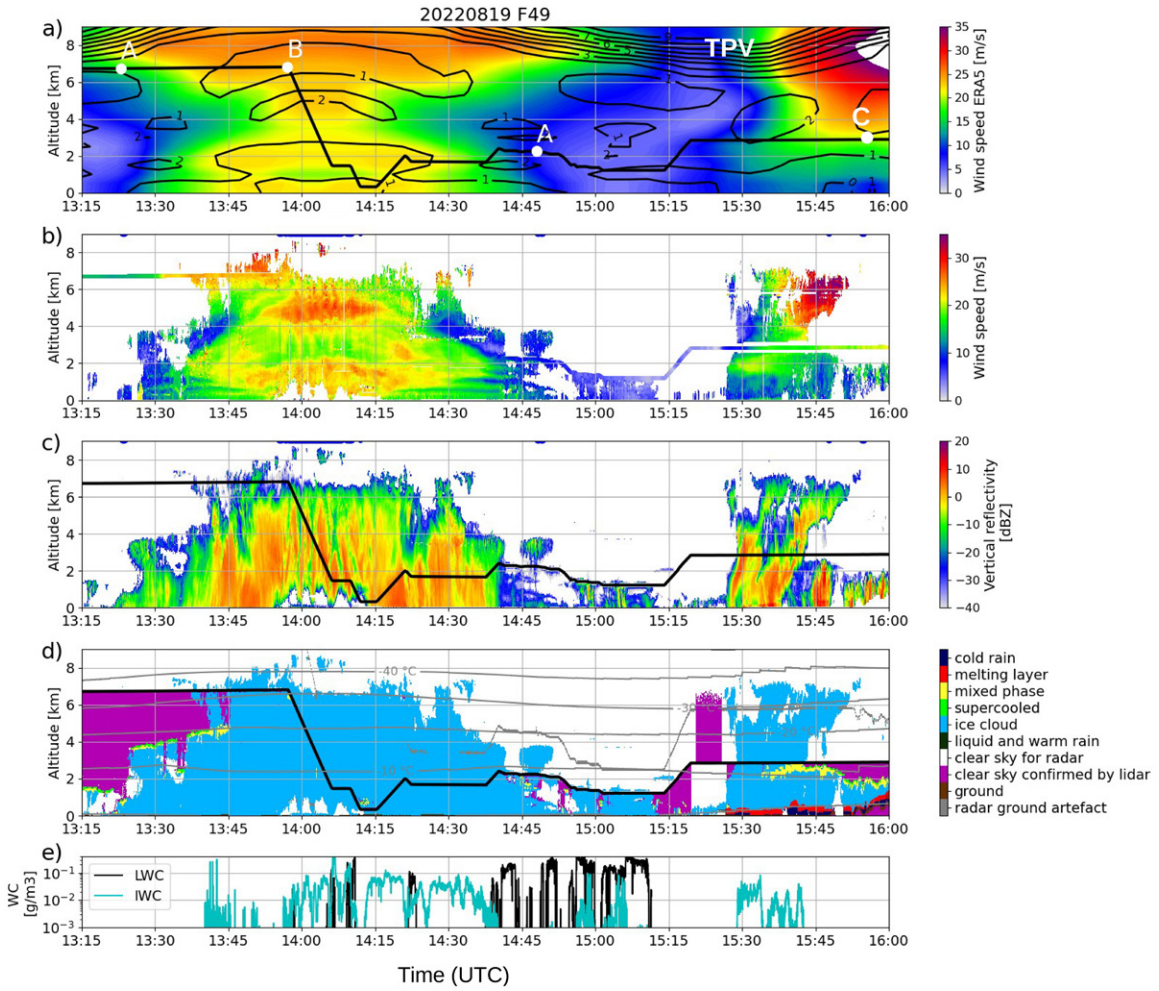

Fig. 13. Dynamical and microphysical properties along flight S49 on 19 Aug 2022 across AC3 during its mature columnar vortex stage. (a) ERA5 wind speed (shading; m s^{-1}) and PV (contour interval 1 PVU). The points A, B, and C are those related to change in the direction of flight S49, as shown in Figs. 12a and 12b. The cross section is obtained using ERA5 hourly datasets and averaging the variables along the flight path with the closest ERA5 grid points. (b) Wind speed from RASTA retrieval and in situ aircraft's measurements. Blue line at the top of the panel illustrates the turns, (c) RASTA reflectivity, (d) RALI synergistic categorization, and (e) in situ IWC and LWC. The TPV center is indicated in white in (a).

RASTA did not measure winds, except close to point B where the RASTA wind speed values are very close to those measured by in situ sensors and to the ERA5 wind speed. Interestingly, a second wind maximum appears at midlevels between 4 and 6 km in both ERA5 and RASTA observations at point B and a third wind maximum appears roughly at the same location just above the boundary layer with peak values also near 22–25 m s^{-1}. The alternation of local maxima in wind speed and reflectivity values between 1400 and 1415 from a 6-km height down to the surface (Figs. 13b,c) is due to the spiral descent of the aircraft going back and forth through the strong gradient in northerly wind. The upper-level wind is greatest (≥35 m s^{-1}) in the jet observed on the SE flank of the TPV (above point C). While the TPV center itself cannot be observed by radar (due to the absence of scatterers), the upper-tropospheric cyclonic flow around the TPV is observed on both flanks.

Cloud properties are classified using the radar–lidar synergistic retrieval (Fig. 13d) and confirmed by in situ IWC and LWC (Fig. 13e). The deep clouds near point B are categorized as ice clouds (including snow falling from them until 1440 along the flight) except very near the surface where some liquid was detected at around 1410. Between the strongest northerly winds near point B and the center of the columnar vortex, there was a transition to midlevel clouds whose tops are characterized by a layer of supercooled water detected by the lidar

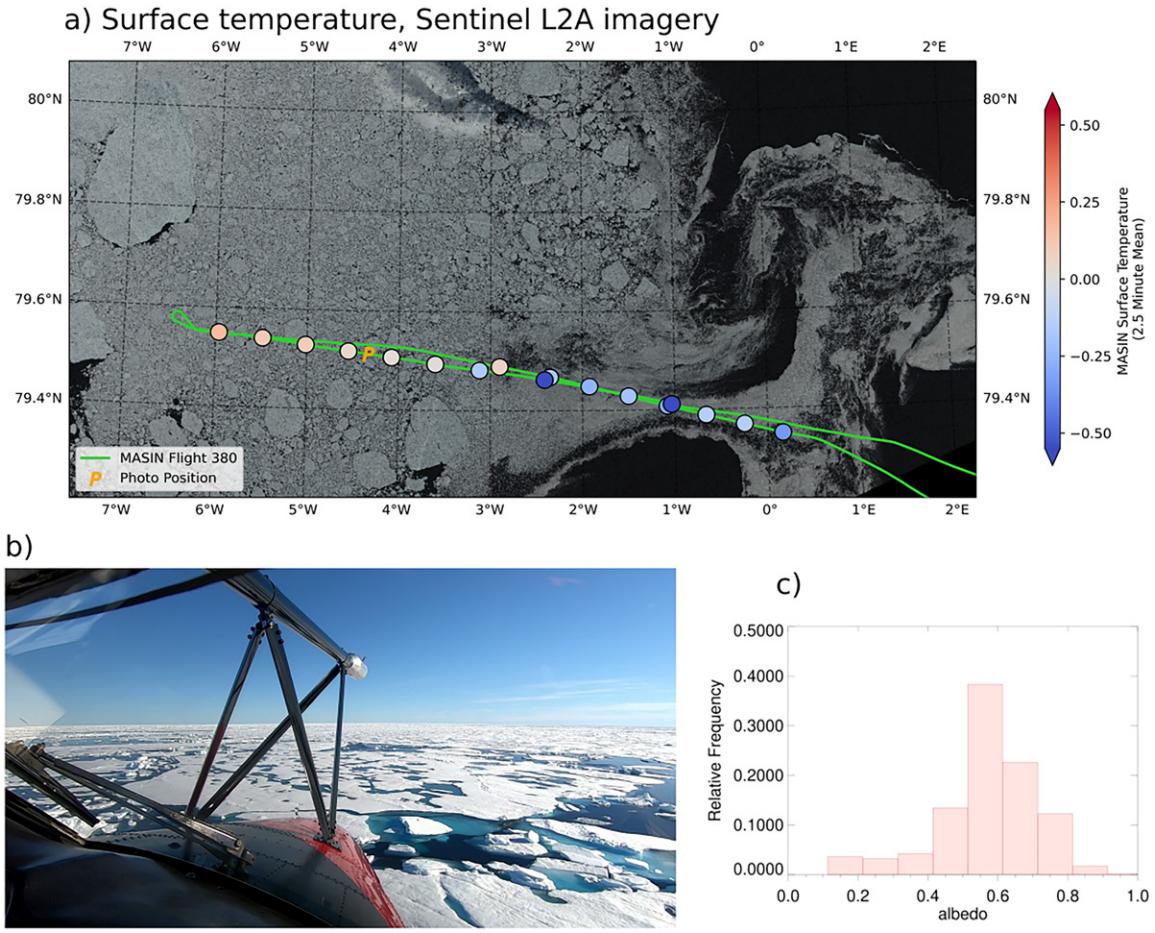

Fig. 14. (a) The track of flight B380 (green) and observed surface temperature (shaded dots) overlain on a Sentinel-2 L2A satellite image of the region at 1448 UTC 20 Aug 2022; (b) photo from flight B380 of the sea ice conditions at 1228 UTC on the same day, heading eastward at position P marked in (a); and (c) histogram of the measured surface albedo over sea ice during the low-level legs of flight B380.

between 1320 and 1345 (Fig. 13d) and by in situ probes near 1445 (Fig. 13e). Between 1450 and 1515, the boundary layer clouds are identified as mixed-phase clouds following the in situ measurements. Between 1520 and 1525, the lidar was pointing upward and did not detect any clouds. Hence, right below the TPV center, there were only very shallow boundary layer clouds. Southeast of the TPV center (near point C), there were deep clouds, mainly formed of ice crystals and the lidar (now pointing downward again) detected supercooled water at midlevel cloud tops (1535–1600).

Figure 14 illustrates the sea ice surface conditions observed during flight B380 to the southwest of the low center and at the southern end of the advected cold air (Fig. 12c). The Sentinel-2 L2A swath passed the region approximately 2.5 h after the aircraft reached its most westerly point. The interior (west) of the sea ice field consists of a densely packed medium to large ice floes, while to the east, the sea ice mostly consists of loosely packed small floes. The overlaid surface temperature measurements are 150 s means of data retrieved from the IR thermometer (Fig. 14a) during low-level legs of flight B380 (at only 50–100 feet above the surface). The values vary between −0.5° and 0.5°C, and, unusually, the warmer surface temperatures are to the west, further into the sea ice where there were more melt ponds on the sea ice, as illustrated in the photo from the aircraft (melt ponds are pale blue, open water leads are much darker). This points to melt pond surface temperatures being above the freezing point over a relatively widespread area.

The histogram displays the broadband (295–2800 nm) albedo measured during flight B380 using SW and LW radiometers, demonstrating the wide range of surface reflectivity

that arises from a mixture of surface types (Fig. 14c). In data along the flight track, melt ponds and leads can be clearly distinguished from the bare ice and snow-covered ice by their albedo signatures and sometimes their temperature (Perovich et al. 2002). Such low-level observations are being used to evaluate models and determine surface exchange parameterization settings.

7. Conclusions

THINICE is the first field campaign dedicated to observing mesoscale features of Arctic cyclones (ACs). During August 2022, four summertime ACs were intensively observed by two research aircraft to explore their detailed structure, evolution, and surface-interaction processes, while WindBorne (WB) balloons were used to explore the links between tropopause polar vortices and surface cyclone development. Cyclone 3 was a prototype of long-lived ACs transitioning from a baroclinic structure to a cold-core columnar vortex. Croad et al. (2023b) have shown recently with a 42-yr climatology that 34% of summertime ACs, and the majority (60%) of ACs lasting more than 9 days, follow this type of evolution. The highlights of the THINICE observations shown here yield the following preliminary results:

- Deep clouds along fronts, embedded within summertime ACs, are mainly ice clouds, while the surrounding midlevel clouds contain supercooled water droplets, quite regularly at the cloud tops but also in some cases within the clouds in multiple thin layers (flight S40). While multiple supercooled water layers have already been observed (e.g., Alexander et al. 2021), this is the first time to our knowledge that remote sensing and in situ measurements on board an aircraft provide a comprehensive view of such layers in the same cloud.
- The easterly low-level jet (LLJ) on the northern flank of cyclone 2 was observed to be confined beneath a sloping frontal surface, running parallel to this bent-back front in the colder air. Therefore, it was similar to the cold conveyor belt frequently observed in mature midlatitude cyclones. The LLJ strength was shown to be underestimated in global analyses and also short-term forecasts of two mesoscale models by up to 5 m s^{-1} when compared to in situ and the RASTA Doppler radar observations. A preliminary study analyzing the jet strength for all four ACs during THINICE shows that this wind speed underestimation in the short-term forecasts or reanalysis is systematic (not shown here), which is quite surprising as such a bias was not found in midlatitude cyclones (Schäfler et al. 2020).
- Heterogeneity in sea ice properties—such as the size of ice floes, the fraction of melt ponds, and the fraction of leads—results in large spatial variability in albedo and surface temperature values in the MIZ. Some operational centers are just beginning to represent such heterogeneities in their coupled forecasting systems and are keen for validation. Our observations are unique as we have been able to measure simultaneous surface-layer meteorology, fluxes, and sea ice characteristics (e.g., sea ice fraction and melt-pond fraction). The interaction between these surface characteristics and the ACs is captured by this novel set of observations, and they are proving valuable in evaluating simulations and tuning model configurations.
- Arctic forecasts, including AC cases, are found to be sensitive to the structure of tropopause polar vortices upstream in the initial conditions by using experiments with and without the assimilation of WB balloon data (see supplemental text and Fig. S1 in the online supplemental material) and by using adjoint and ensemble sensitivity approaches (Fig. S2).

Thanks to the complementarity of the observational platforms and a fortuitous high occurrence of ACs within a range of Svalbard in August 2022, the THINICE observations provide a unique dataset to study ACs and their interactions with clouds, boundary layer turbulence,

and the sea ice surface. The most novel aspects of the THINICE observations are the relatively long aircraft transects measuring the variability in cloud properties in relation to cyclone wind structure and also the contemporaneous measurement of turbulent fluxes in the surface layer above sea ice in both melting and freezing conditions. Two particular directions of model development will be investigated in the future: one concerns the representation of Arctic mixed-phase cloud and the second topic relates to the parameterization of subgrid variability in sea ice properties influencing the surface energy budget and representation of momentum transfer between the ice and atmosphere.

Acknowledgments. ATR42 Airborne data were obtained using the aircraft managed by Safire, the French facility for airborne research, an infrastructure of the French National Center for Scientific Research (CNRS), Météo-France, and the French National Center for Space Studies (CNES). The deployment of the Safire ATR42 aircraft was funded by the Office of Naval Research (ONR) Departmental Research Initiative (DRI), through the RALI-THINICE project, and also by Centre National Etudes Spatiales (CNES) via the project entitled "Expecting Earth-Care, Learning from A-Train" (E-ECLAT) and CNRS via its program INSU-LEFE. The RALI platform attached to OVSQ and the cloud microphysics in situ platform (PMA) attached to LaMP/OPGC are both National Instruments of INSU. The data center "Données et Services pour l'Atmosphère" (AERIS) and its teams are also deeply acknowledged for their constant support. The British Antarctic Survey Twin Otter aircraft flights and the participation by the U.K. team were funded by the Natural Environment Research Council (NERC) as part of the Arctic Summertime Cyclones project (NE/T006773/1, NE/T006811/1, and NE/T00682X/1). The NRL team gratefully acknowledges support from the ONR Program Element (PE) 0601153N Arctic Cyclone Department Research Initiative and ONR PE 0602435N. Hannah Croad and Miriam Bennett were funded by NERC PhD studentships. The campaign would not have been possible without the skills, experience, and dedication of the pilots and aircraft engineers of the BAS Twin Otter (Andrew van Kints, Alan Howland, and Liam Tranter) and the Safire ATR42 aircraft. The Met Office and Paul Field and Melissa Brooks, in particular, are acknowledged for their support in terms of forecasts and for making the RAL3 experimental forecasts available in real time and during the preparation of this article.

Data availability statement. The THINICE observed datasets of the Safire ATR42 flights can be accessed in the RALI-THINICE field campaign: https://ralithinice.aeris-data.fr/data-catalog/. The BAS MASIN Arctic Summertime Cyclones flight data are archived at the Centre for Environmental Data Analysis (CEDA) at https://data.ceda.ac.uk/badc/arcticcyclones. The THINICE observed data from all WindBorne balloon flights are available via https://windbornesystems.com/access_requests/new. Met Office operational analyses shown can be obtained from the TIGGE archive (https://www.ecmwf.int/en/research/projects/tigge), and the regional forecasts using the RAL3 science configuration of the MetUM are archived on the Met Office MASS archive. AROME forecasts presented in Fig. 9 are experiments made at CNRM/GMAP (Météo-France, Toulouse) and are available at https://observations.ipsl.fr/aeris/rali/.

References

Aizawa, T., and H. L. Tanaka, 2016: Axisymmetric structure of the long lasting summer Arctic cyclones. *Polar Sci.*, **10**, 192–198, https://doi.org/10.1016/j.polar.2016.02.002.

Alexander, S. P., G. M. McFarquhar, R. Marchand, A. Protat, E. Vignon, G. G. Mace, and A. R. Klekociuk, 2021: Mixed-phase clouds and precipitation in Southern Ocean Cyclones and cloud systems observed poleward of 64°S by ship-based cloud radar and lidar. *J. Geophys. Res. Atmos.*, **126**, e2020JD033626, https://doi.org/10.1029/2020JD033626.

Asplin, M. G., R. Galley, D. G. Barber, and S. Prinsenberg, 2012: Fracture of summer perennial sea ice by ocean swell as a result of Arctic storms. *J. Geophys. Res.*, **117**, C06025, https://doi.org/10.1029/2011JC007221.

Aue, L., T. Vihma, P. Uotila, and A. Rinke, 2022: New insights into cyclone impacts on sea ice in the Atlantic sector of the Arctic Ocean in winter. *Geophys. Res. Lett.*, **49**, e2022GL100051, https://doi.org/10.1029/2022GL100051.

Brousseau, P., Y. Seity, D. Ricard, and J. Léger, 2016: Improvement of the forecast of convective activity from the AROME-France system. *Quart. J. Roy. Meteor. Soc.*, **142**, 2231–2243, https://doi.org/10.1002/qj.2822.

Brümmer, B., D. Schroder, G. Muller, G. Spreen, A. Jahnke-Bornemann, and J. Launiainen, 2008: Impact of a Fram Strait cyclone on ice edge, drift, divergence, and concentration: Possibilities and limits of an observational analysis. *J. Geophys. Res.*, **113**, C12003, https://doi.org/10.1029/2007JC004149.

Bruneau, D., and Coauthors, 2015: 355-nm high spectral resolution airborne lidar LNG: System description and first results. *Appl. Opt.*, **54**, 8776–8785, https://doi.org/10.1364/AO.54.008776.

Bush, M., and Coauthors, 2023: The second Met Office Unified Model–JULES Regional Atmosphere and Land configuration, RAL2. *Geosci. Model Dev.*, **16**, 1713–1734, https://doi.org/10.5194/gmd-16-1713-2023.

Cai, Y., D. C. Montague, W. Mooiweer-Bryan, and T. Deshler, 2008: Performance characteristics of the ultra high sensitivity aerosol spectrometer for particles between 55 and 800 nm: Laboratory and field studies. *J. Aerosol Sci.*, **39**, 759–769, https://doi.org/10.1016/j.jaerosci.2008.04.007.

Capute, P. K., and R. D. Torn, 2021: A comparison of Arctic and Atlantic cyclone predictability. *Mon. Wea. Rev.*, **149**, 3837–3849, https://doi.org/10.1175/MWR-D-20-0350.1.

Cavallo, S. M., and G. J. Hakim, 2010: Composite structure of tropopause polar cyclones. *Mon. Wea. Rev.*, **138**, 3840–3857, https://doi.org/10.1175/2010MWR3371.1.

Cazenave, Q., M. Ceccaldi, J. Delanoë, J. Pelon, S. Groß, and A. Heymsfield, 2019: Evolution of DARDAR-CLOUD ice cloud retrievals: New parameters and impacts on the retrieved microphysical properties. *Atmos. Meas. Tech.*, **12**, 2819–2835, https://doi.org/10.5194/amt-12-2819-2019.

Ceccaldi, M., J. Delanoë, R. J. Hogan, N. L. Pounder, A. Protat, and J. Pelon, 2013: From CloudSat-CALIPSO to EarthCare: Evolution of the DARDAR cloud classification and its comparison to airborne Radar-Lidar observations. *J. Geophys. Res. Atmos.*, **118**, 7962–7981, https://doi.org/10.1002/jgrd.50579.

Clancy, R., C. M. Bitz, E. Blanchard-Wrigglesworth, M. C. McGraw, and S. M. Cavallo, 2022: A cyclone-centered perspective on the drivers of asymmetric patterns in the atmosphere and sea ice during Arctic cyclones. *J. Climate*, **35**, 73–89, https://doi.org/10.1175/JCLI-D-21-0093.1.

Crawford, A. D., J. V. Lukovich, M. R. McCrystall, J. C. Stroeve, and D. G. Barber, 2022: Reduced sea ice enhances intensification of winter storms over the Arctic Ocean. *J. Climate*, **35**, 3353–3370, https://doi.org/10.1175/JCLI-D-21-0747.1.

Croad, H. L., J. Methven, B. Harvey, S. P. E. Keeley, and A. Volonté, 2023a: The role of boundary layer processes in summer-time Arctic cyclones. *Wea. Climate Dyn.*, **4**, 617–638, https://doi.org/10.5194/wcd-4-617-2023.

——, ——, ——, ——, ——, and K. I. Hodges, 2023b: A climatology of summer-time Arctic cyclones using a modified phase space. *Geophys. Res. Lett.*, **50**, e2023GL105993, https://doi.org/10.1029/2023GL105993.

Day, J. J., and K. I. Hodges, 2018: Growing land-sea temperature contrast and the intensification of Arctic cyclones. *Geophys. Res. Lett.*, **45**, 3673–3681, https://doi.org/10.1029/2018GL077587.

——, and Coauthors, 2024: The Year of Polar Prediction site Model Intercomparison Project (YOPPsiteMIP) phase 1: Project overview and Arctic winter forecast evaluation. *Geosci. Model Dev.*, **17**, 5511–5543, https://doi.org/10.5194/gmd-17-5511-2024.

Dean, J., and J. Creus-Costa, 2021: Windborne THINICE report. Tech. Rep., 15 pp., https://a.windbornesystems.com/syzygy/eclipse_fdfmqd/report.pdf.

Dearden, C., G. Vaughan, T. Tsai, and J.-P. Chen, 2016: Exploring the diabatic role of ice microphysical processes in two North Atlantic summer cyclones. *Mon. Wea. Rev.*, **144**, 1249–1272, https://doi.org/10.1175/MWR-D-15-0253.1.

Delanoë, J., and R. J. Hogan, 2008: A variational scheme for retrieving ice cloud properties from combined radar, lidar, and infrared radiometer. *J. Geophys. Res.*, **113**, D07204, https://doi.org/10.1029/2007JD009000.

——, A. Protat, O. Jourdan, J. Pelon, M. Papazonni, R. Dupuy, J.-F. Gayet, and C. Jouan, 2013: Comparison of airborne in situ, airborne radar–lidar, and spaceborne radar–lidar retrievals of polar ice cloud properties sampled during the POLARCAT campaign. *J. Atmos. Oceanic Technol.*, **30**, 57–73, https://doi.org/10.1175/JTECH-D-11-00200.1.

——, and Coauthors, 2016: BASTA: A 95-GHz FMCW Doppler radar for cloud and fog studies. *J. Atmos. Oceanic Technol.*, **33**, 1023–1038, https://doi.org/10.1175/JTECH-D-15-0104.1.

Ehrlich, A., and Coauthors, 2019: A comprehensive in situ and remote sensing data set from the Arctic CLoud Observations Using airborne measurements during polar Day (ACLOUD) campaign. *Earth Syst. Sci. Data*, **11**, 1853–1881, https://doi.org/10.5194/essd-11-1853-2019.

Elvidge, A. D., I. A. Renfrew, A. I. Weiss, I. M. Brooks, T. A. Lachlan-Cope, and J. C. King, 2016: Observations of surface momentum exchange over the marginal ice zone and recommendations for its parametrisation. *Atmos. Chem. Phys.*, **16**, 1545–1563, https://doi.org/10.5194/acp-16-1545-2016.

——, ——, I. M. Brooks, P. Srivastava, M. J. Yelland, and J. Prytherch, 2021: Surface heat and moisture exchange in the marginal ice zone: Observations and a new parameterization scheme for weather and climate models. *J. Geophys. Res. Atmos.*, **126**, e2021JD034827, https://doi.org/10.1029/2021JD034827.

——, ——, J. M. Edwards, I. M. Brooks, P. Srivastava, and A. I. Weiss, 2023: Improved simulation of the polar atmospheric boundary layer by accounting for aerodynamic roughness in the parameterization of surface scalar exchange over sea ice. *J. Adv. Model. Earth Syst.*, **15**, e2022MS003305, https://doi.org/10.1029/2022MS003305.

Fearon, M. G., J. D. Doyle, D. R. Ryglicki, P. M. Finocchio, and M. Sprenger, 2021: The role of cyclones in moisture transport into the Arctic. *Geophys. Res. Lett.*, **48**, e2020GL090353, https://doi.org/10.1029/2020GL090353.

Field, P., and Coauthors, 2023: Implementation of a double moment cloud microphysics scheme in the UK Met Office regional numerical weather prediction model. *Quart. J. Roy. Meteor. Soc.*, **149**, 703–739, https://doi.org/10.1002/qj.4414.

Finocchio, P. M., J. D. Doyle, and D. P. Stern, 2022: Accelerated sea ice loss from late summer cyclones in the New Arctic. *J. Climate*, **35**, 7751–7769, https://doi.org/10.1175/JCLI-D-22-0315.1.

Ford, J. D., T. Pearce, I. V. Canosa, and S. Harper, 2021: The rapidly changing Arctic and its societal implications. *Wiley Interdiscip. Rev.: Climate Change*, **12**, e735, https://doi.org/10.1002/wcc.735.

Gayet, J. F., O. Crépel, J. F. Fournol, and S. Oshchepkov, 1997: A new airborne polar Nephelometer for the measurements of optical and microphysical cloud properties. Part I: Theoretical design. *Ann. Geophys.*, **15**, 451–459, https://doi.org/10.1007/s00585-997-0451-1.

Gray, S. L., K. I. Hodges, J. L. Vautrey, and J. Methven, 2021: The role of tropopause polar vortices in the intensification of summer Arctic cyclones. *Wea. Climate Dyn.*, **2**, 1303–1324, https://doi.org/10.5194/wcd-2-1303-2021.

Hersbach, H., and Coauthors, 2020: The ERA5 global reanalysis. *Quart. J. Roy. Meteor. Soc.*, **146**, 1999–2049, https://doi.org/10.1002/qj.3803.

Hodges, K. I., 1994: A general method for tracking analysis and its application to meteorological data. *Mon. Wea. Rev.*, **122**, 2573–2586, https://doi.org/10.1175/1520-0493(1994)122<2573:AGMFTA>2.0.CO;2.

——, 1995: Feature tracking on the unit sphere. *Mon. Wea. Rev.*, **123**, 3458–3465, https://doi.org/10.1175/1520-0493(1995)123<3458:FTOTUS>2.0.CO;2.

——, 1999: Adaptive constraints for feature tracking. *Mon. Wea. Rev.*, **127**, 1362–1373, https://doi.org/10.1175/1520-0493(1999)127<1362:ACFFT>2.0.CO;2.

Hofer, S., A. J. Tedstone, X. Fettweis, and J. L. Bamber, 2019: Cloud microphysics and circulation anomalies control differences in future Greenland melt. *Nat. Climate Change*, **9**, 523–528, https://doi.org/10.1038/s41558-019-0507-8.

Inoue, J., and M. Hori, 2011: Arctic cyclogenesis at the marginal ice zone: A contributory mechanism for the temperature amplification? *Geophys. Res. Lett.*, **38**, L12502, https://doi.org/10.1029/2011GL047696.

Itkin, P., and Coauthors, 2016: Thin ice and storms: Sea ice deformation from buoy arrays deployed during N-ICE2015. *J. Geophys. Res. Oceans*, **122**, 4661–4674, https://doi.org/10.1002/2016JC012403.

Jakobson, L., T. Vihma, E. Jakobson, T. Palo, A. Männik, and J. Jaagus, 2013: Low-level jet characteristics over the Arctic Ocean in spring and summer. *Atmos. Chem. Phys.*, **13**, 11 089–11 099, https://doi.org/10.5194/acp-13-11089-2013.

Kay, J. E., C. Wall, V. Yettella, B. Medeiros, C. Hannay, P. Caldwell, and C. Bitz, 2016: Global climate impacts of fixing the Southern Ocean shortwave radiation bias in the Community Earth System Model (CESM). *J. Climate*, **29**, 4617–4636, https://doi.org/10.1175/JCLI-D-15-0358.1.

Køltzow, M., B. Casati, E. Bazile, T. Haiden, and T. Valkonen, 2019: An NWP model intercomparison of surface weather parameters in the European Arctic during the year of polar prediction special observing period Northern Hemisphere 1. *Wea. Forecasting*, **34**, 959–983, https://doi.org/10.1175/WAF-D-19-0003.1.

Korolev, A., and Coauthors, 2017: Mixed-phase clouds: Progress and challenges. *Ice Formation and Evolution in Clouds and Precipitation: Measurement and Modeling Challenges*, *Meteor. Monogr.*, No. 58, Amer. Meteor. Soc., https://doi.org/10.1175/AMSMONOGRAPHS-D-17-0001.1.

Lance, S., C. A. Brock, D. Rogers, and J. A. Gordon, 2010: Water droplet calibration of the Cloud Droplet Probe (CDP) and in-flight performance in liquid, ice and mixed-phase clouds during ARCPAC. *Atmos. Meas. Tech.*, **3**, 1683–1706, https://doi.org/10.5194/amt-3-1683-2010.

Lawson, R. P., R. E. Stewart, J. W. Strapp, and G. A. Isaac, 1993: Aircraft observations of the origin and growth of very large snowflakes. *Geophys. Res. Lett.*, **20**, 53–56, https://doi.org/10.1029/92GL02917.

——, D. O'Connor, P. Zmarzly, K. Weaver, B. Baker, Q. Mo, and H. Jonsson, 2006: The 2D-S (Stereo) probe: Design and preliminary tests of a new airborne, high-speed, high-resolution particle imaging probe. *J. Atmos. Oceanic Technol.*, **23**, 1462–1477, https://doi.org/10.1175/JTECH1927.1.

López-García, V., R. R. Neely III, S. Dahlke, and I. M. Brooks, 2022: Low-level jets over the Arctic Ocean during MOSAiC. *Elementa*, **10**, 00063, https://doi.org/10.1525/elementa.2022.00063.

Luo, Y., K.-M. Xu, H. Morrison, G. M. McFarquhar, Z. Wang, and G. Zhang, 2008: Multi-layer Arctic mixed-phase clouds simulated by a cloud-resolving model: Comparison with ARM observations and sensitivity experiments. *J. Geophys. Res.*, **113**, D12208, https://doi.org/10.1029/2007JD009563.

Lüpkes, C., V. M. Gryanik, A. Rösel, G. Birnbaum, and L. Kaleschke, 2013: Effect of sea ice morphology during Arctic summer on atmospheric drag coefficients used in climate models. *Geophys. Res. Lett.*, **40**, 446–451, https://doi.org/10.1002/grl.50081.

Mazoyer, M., and Coauthors, 2021: Microphysics impacts on the warm conveyor belt and ridge building of the NAWDEX IOP6 cyclone. *Mon. Wea. Rev.*, **149**, 3961–3980, https://doi.org/10.1175/MWR-D-21-0061.1.

——, D. Ricard, G. Rivière, J. Delanoë, S. Riette, C. Augros, M. Borderies, and B. Vié, 2023: Impact of mixed-phase cloud parameterization on warm conveyor belts and upper-tropospheric dynamics. *Mon. Wea. Rev.*, **151**, 1073–1091, https://doi.org/10.1175/MWR-D-22-0045.1.

Mech, M., and Coauthors, 2022: MOSAiC-ACA and AFLUX—Arctic airborne campaigns characterizing the exit area of MOSAiC. *Sci. Data*, **9**, 790, https://doi.org/10.1038/s41597-022-01900-7.

Meier, W. N., and Coauthors, 2022: Sea ice [in "state of the climate in 2021"]. *Bull. Amer. Meteor. Soc.*, **103**, S270–S273, https://doi.org/10.1175/BAMS-D-22-0082.1.

Mioche, G., O. Jourdan, M. Ceccaldi, and J. Delanoë, 2015: Variability of mixed-phase clouds in the Arctic with a focus on the Svalbard region: A study based on spaceborne active remote sensing. *Atmos. Chem. Phys.*, **15**, 2445–2461, https://doi.org/10.5194/acp-15-2445-2015.

Mioduszewski, J., S. Vavrus, and M. Wang, 2018: Diminishing Arctic sea ice promotes stronger surface winds. *J. Climate*, **31**, 8101–8119, https://doi.org/10.1175/JCLI-D-18-0109.1.

Morrison, H., and Coauthors, 2009: Intercomparison of model simulations of mixed-phase clouds observed during the ARM Mixed-Phase Arctic Cloud Experiment. II: Multilayer cloud. *Quart. J. Roy. Meteor. Soc.*, **135**, 1003–1019, https://doi.org/10.1002/qj.415.

——, G. de Boer, G. Feingold, J. Harrington, M. D. Shupe, and K. Sulia, 2012: Resilience of persistent Arctic mixed-phase clouds. *Nat. Geosci.*, **5**, 11–17, https://doi.org/10.1038/ngeo1332.

Oertel, A., A. K. Miltenberger, C. M. Grams, and C. Hoose, 2023: Interaction of microphysics and dynamics in a warm conveyor belt simulated with the ICOsahedral Nonhydrostatic (ICON) model. *Atmos. Chem. Phys.*, **23**, 8553–8581, https://doi.org/10.5194/acp-23-8553-2023.

Oltmanns, M., F. Straneo, and M. Tedesco, 2019: Increased Greenland melt triggered by large-scale, year-round cyclonic moisture intrusions. *Cryosphere*, **13**, 815–825, https://doi.org/10.5194/tc-13-815-2019.

Overland, J. E., M. Wang, J. E. Walsh, and J. C. Stroeve, 2014: Future Arctic climate changes: Adaptation and mitigation time scales. *Earth's Future*, **2**, 68–74, https://doi.org/10.1002/2013EF000162.

Perovich, D. K., T. C. Grenfell, B. Light, and P. V. Hobbs, 2002: Seasonal evolution of the albedo of multiyear Arctic sea ice. *J. Geophys. Res.*, **107**, 8044, https://doi.org/10.1029/2000JC000438.

Persson, P. O. G., 2010: Summary of meteorological conditions during the Arctic Mechanisms for the Interaction of the Surface and Atmosphere (AMISA) intensive observation periods. NOAA Technical Memorandum OAR PSD, U.S. Department of Commerce, National Oceanic and Atmospheric Administration, Office of Oceanic and Atmospheric Research, Earth System Research Laboratory, Physical Sciences Division, 57 pp., https://books.google.fr/books?id=XZorugEACAAJ.

——, 2012: Onset and end of the summer melt season over sea ice: Thermal structure and surface energy perspective from SHEBA. *Climate Dyn.*, **39**, 1349–1371, https://doi.org/10.1007/s00382-011-1196-9.

——, M. D. Shupe, D. Perovich, and A. Solomon, 2017: Linking atmospheric synoptic transport, cloud phase, surface energy fluxes, and sea-ice growth: Observations of midwinter SHEBA conditions. *Climate Dyn.*, **49**, 1341–1364, https://doi.org/10.1007/s00382-016-3383-1.

——, and Coauthors, 2018: Shipboard observations of the meteorology and near-surface environment during autumn freezeup in the Beaufort/Chukchi seas. *J. Geophys. Res. Oceans*, **123**, 4930–4969, https://doi.org/10.1029/2018JC013786.

Post, E., and Coauthors, 2013: Ecological consequences of sea-ice decline. *Science*, **341**, 519–524, https://doi.org/10.1126/science.1235225.

Raillard, L., and Coauthors, 2024: Leveraging RALI-THINICE observations to assess how the ICOLMDZ model simulates clouds embedded in Arctic cyclones. *J. Geophys. Res. Atmos.*, **129**, e2024JD040973, https://doi.org/10.1029/2024JD040973.

Renfrew, I. A., A. D. Elvidge, and J. M. Edwards, 2019: Atmospheric sensitivity to marginal-ice-zone drag: Local and global responses. *Quart. J. Roy. Meteor. Soc.*, **145**, 1165–1179, https://doi.org/10.1002/qj.3486.

Ruffieux, D., P. O. G. Persson, C. W. Fairall, and D. E. Wolfe, 1995: Ice pack and lead surface energy budgets during LEADEX 1992. *J. Geophys. Res.*, **100**, 4593–4612, https://doi.org/10.1029/94JC02485.

Schäfler, A., B. Harvey, J. Methven, J. D. Doyle, S. Rahm, O. Reitebuch, F. Weiler, and B. Witschas, 2020: Observation of jet stream winds during NAWDEX and characterization of systematic meteorological analysis errors. *Mon. Wea. Rev.*, **148**, 2889–2907, https://doi.org/10.1175/MWR-D-19-0229.1.

Seity, Y., P. Brousseau, S. Malardel, G. Hello, P. Bénard, F. Bouttier, C. Lac, and V. Masson, 2011: The AROME-France convective-scale operational model. *Mon. Wea. Rev.*, **139**, 976–991, https://doi.org/10.1175/2010MWR3425.1.

Serreze, M. C., 1995: Climatological aspects of cyclone development and decay in the Arctic. *Atmos.–Ocean*, **33** (1), 1–23, https://doi.org/10.1080/07055900.1995.9649522.

——, and R. G. Barry, 1988: Synoptic activity in the Arctic basin, 1979–85. *J. Climate*, **1**, 1276–1295, https://doi.org/10.1175/1520-0442(1988)001<1276:SAITAB>2.0.CO;2.

——, and A. P. Barrett, 2008: The summer cyclone maximum over the central Arctic Ocean. *J. Climate*, **21**, 1048–1065, https://doi.org/10.1175/2007JCLI1810.1.

——, A. H. Lynch, and M. P. Clark, 2001: The Arctic frontal zone as seen in the NCEP–NCAR reanalysis. *J. Climate*, **14**, 1550–1567, https://doi.org/10.1175/1520-0442(2001)014<1550:TAFZAS>2.0.CO;2.

Shupe, M. D., and J. M. Intrieri, 2004: Cloud radiative forcing of the Arctic surface: The influence of cloud properties, surface albedo, and solar zenith angle. *J. Climate*, **17**, 616–628, https://doi.org/10.1175/1520-0442(2004)017<0616:CRFOTA>2.0.CO;2.

——, and Coauthors, 2022: Overview of the MOSAiC expedition: Atmosphere. *Elementa*, **10**, 00060, https://doi.org/10.1525/elementa.2021.00060.

Simmonds, I., and I. Rudeva, 2012: The Great Arctic Cyclone of August 2012. *Geophys. Res. Lett.*, **39**, L23709, https://doi.org/10.1029/2012GL054259.

——, and ——, 2014: A comparison of tracking methods for extreme cyclones in the Arctic basin. *Tellus*, **66A**, 25252, https://doi.org/10.3402/tellusa.v66.25252.

Smith, M., and Coauthors, 2018: Episodic reversal of autumn ice advance caused by release of ocean heat in the Beaufort Sea. *J. Geophys. Res. Oceans*, **123**, 3164–3185, https://doi.org/10.1002/2018JC013764.

Solomon, A., M. D. Shupe, P. O. G. Persson, and H. Morrison, 2011: Moisture and dynamical interactions maintaining decoupled Arctic Mixed-Phase Stratocumulus in the presence of a humidity inversion. *Atmos. Chem. Phys.*, **11**, 10127–10148, https://doi.org/10.5194/acp-11-10127-2011.

Sotiropoulou, G., J. Sedlar, R. Forbes, and M. Tjernström, 2016: Summer Arctic clouds in the ECMWF forecast model: An evaluation of cloud parametrization schemes. *Quart. J. Roy. Meteor. Soc.*, **142**, 387–400, https://doi.org/10.1002/qj.2658.

Spreen, G., L. Kaleschke, and G. Heygster, 2008: Sea ice remote sensing using AMSR-E 89-GHz channels. *J. Geophys. Res.*, **113**, C02S03, https://doi.org/10.1029/2005JC003384.

Tanaka, H. L., A. Yamagami, and S. Takahashi, 2012: The structure and behavior of the arctic cyclone in summer analyzed by the JRA-25/JCDAS data. *Polar Sci.*, **6**, 55–69, https://doi.org/10.1016/j.polar.2012.03.001.

Tilinina, N., S. K. Gulev, and D. H. Bromwich, 2014: New view of Arctic cyclone activity from the Arctic system reanalysis. *Geophys. Res. Lett.*, **41**, 1766–1772, https://doi.org/10.1002/2013GL058924.

Tjernström, M., and Coauthors, 2014: The Arctic Summer Cloud Ocean Study (ASCOS): Overview and experimental design. *Atmos. Chem. Phys.*, **14**, 2823–2869, https://doi.org/10.5194/acp-14-2823-2014.

Uccelini, L. W., 1990: Processes contributing to the rapid development of extratropical cyclones. *Extratropical Cyclones*, C. W. Newton and E. O. Holopainen, Eds., Amer. Meteor. Soc., 81–105.

Vessey, A. F., K. I. Hodges, L. C. Shaffrey, and J. J. Day, 2020: An inter-comparison of Arctic synoptic scale storms between four global reanalysis datasets. *Climate Dyn.*, **54**, 2777–2795, https://doi.org/10.1007/s00382-020-05142-4.

——, ——, ——, and ——, 2022: The composite development and structure of intense synoptic-scale Arctic cyclones. *Wea. Climate Dyn.*, **3**, 1097–1112, https://doi.org/10.5194/wcd-3-1097-2022.

Vichi, M., and Coauthors, 2019: Effects of an explosive polar cyclone crossing the Antarctic marginal ice zone. *Geophys. Res. Lett.*, **46**, 5948–5958, https://doi.org/10.1029/2019GL082457.

Vihma, T., J. Hartmann, and C. Lüpkes, 2003: A case study of an on-ice air flow over the Arctic marginal sea-ice zone. *Bound.-Layer Meteor.*, **107**, 189–217, https://doi.org/10.1023/A:1021599601948.

Wendisch, M., and Coauthors, 2024: Overview: Quasi-Lagrangian observations of Arctic air mass transformations—Introduction and initial results of the HALO–$(\mathcal{AC})^3$ aircraft campaign. *Atmos. Chem. Phys.*, **24**, 8865–8892, https://doi.org/10.5194/acp-24-8865-2024.

Yamagami, A., M. Matsueda, and H. L. Tanaka, 2018a: Medium-range forecast skill for extraordinary Arctic cyclones in summer of 2008–2016. *Geophys. Res. Lett.*, **45**, 4429–4437, https://doi.org/10.1029/2018GL077278.

——, ——, and ——, 2018b: Predictability of the 2012 Great Arctic Cyclone on medium-range timescales. *Polar Sci.*, **15**, 13–23, https://doi.org/10.1016/j.polar.2018.01.002.

Yamazaki, A., J. Inoue, K. Dethloff, M. Maturilli, and G. König-Langlo, 2015: Impact of radiosonde observations on forecasting summertime Arctic cyclone formation. *J. Geophys. Res. Atmos.*, **120**, 3249–3273, https://doi.org/10.1002/2014JD022925.

Zhang, J., R. Lindsay, A. Schweiger, and M. Steele, 2013: The impact of an intense summer cyclone on 2012 Arctic sea ice retreat. *Geophys. Res. Lett.*, **40**, 720–726, https://doi.org/10.1002/grl.50190.

Zhang, X., J. E. Walsh, J. Zhang, U. S. Bhatt, and M. Ikeda, 2004: Climatology and interannual variability of Arctic cyclone activity: 1948–2002. *J. Climate*, **17**, 2300–2317, https://doi.org/10.1175/1520-0442(2004)017<2300:CAIVOA>2.0.CO;2.